IRAQI JOURNAL OF APPLIED PHYSICS

The *Iraqi Journal of Applied Physics (IJAP)* is a peer reviewed journal of high quality devoted to the publication of original research papers from applied physics and their broad range of applications. IJAP publishes quality original research papers, comprehensive review articles, survey articles, book reviews, dissertation abstracts in physics and its applications in the broadest sense. It is intended that the journal may act as an interdisciplinary forum for Physics and its applications. Innovative applications and material that brings together diverse areas of Physics are particularly welcome. Review articles in selected areas are published from time to time. It aims to disseminate knowledge; provide a learned reference in the field; and establish channels of communication between academic and research experts, policy makers and executives in industry, commerce and investment institutions. IJAP is a quarterly specialized periodical dedicated to publishing original papers, letters and reviews in: Applied & Nonlinear Optics, Applied Mechanics & Thermodynamics, Digital & Optical Communications, Electronic Materials & Devices, Laser Physics & Applications, Plasma Physics & Applications, Quantum Physics & Spectroscopy, Semiconductors & Optoelectronics, Solid State Physics & Applications, Alternative and Renewable Energy, and Computers and Networks.

ISSN (Print): 1813-2065, ISSN (Online): 2309-1673, ISSN (Letters): 1999-656X

EDITORIAL BOARD

Raad A. KHAMIS	Asst. Professor	Editor-in-Chief	Plasma Physics	IRAQ
Walid K. HAMOUDI	Professor	Member	Laser Physics	IRAQ
Dayah N. RAOUF	Asst. Professor	Member	Laser and Optics	IRAQ
Raid A. ISMAIL	Professor	Member	Semiconductor Physics	IRAQ
Oday A. HAMMADI	Asst. Professor	Managing Editor	Molecular Physics	IRAQ
Intesar F. RAMLEY	Professor	Member	Communications Eng.	CANADA
Manal J. AL-KINDY	Asst. Professor	Member	Electrical Engineering	IRAQ
Khaled A. AHMED	Professor	Member	Theoretical Physics	IRAQ
Kais A. AL-NAIMEE	Asst. Professor	Member	Quantum Optics	ITALY
Abdulmajeed IBRAHIM	Professor	Member	Solid State Physics	IRAQ
Loay E. GEORGE	Asst. Professor	Member	Computers & Networks	IRAQ
Abdulhadi ALKHALILI	Professor	Member	Medical Physics	U.S.A
Haitham M. MIKHLIF	Lecturer	Member	Molecular Physics	IRAQ

Editorial Office:
P. O. Box 55259, Baghdad 12001, IRAQ
Website: www.iraqiphysicsjournal.com
Emails: info@iraqiphysicsjournal.com, editor_ijap@yahoo.co.uk, ijap.editor@gmail.com,

ADVISORY BOARD

Abdullah M. SUHAIL, Professor, Department of Physics, College of Science, University of Baghdad,	IRAQ
Adel K. HAMOUDI, Professor, Department of Physics, College of Science, University of Baghdad,	IRAQ
Andrei KASIMOV, Professor, Institute of Material Science, National Academy of Science, Kiev,	UKRAINE
Ashok KUMAR, Professor, Harcourt Butler Technological Institute, Kanpur, Uttar Pradesh 208 002,	INDIA
Chang Hee NAM, Professor, Korean Advanced Institute of Science and Technology, Daehak-ro, Daejeon,	KOREA
Claudia GAULTIERRE, Professor, Faculty of Sciences and Techniques, University of Rouen, Rouen,	FRANCE
El-Sayed M. FARAG, Professor, Department of Sciences, College of Engineering, AlMinofiya University,	EGYPT
Gang XU, Assistant Professor, Department of Engineering and Physics, University of Central Oklahoma,	U.S.A
Heidi ABRAHAMSE, Professor, Faculty of Health Sciences, University of Johannesburg,	S. AFRICA
Madis-Lipp KROKALMA, Professor, School of Science, Tallinn University of Technology, 19086 Tallinn,	ESTONIA
Mansoor SHEIK-BAHAE, Associate Professor, Department of Physics, University of New Mexico,	U.S.A
Mohammad Robi HOSSAN, Assistant Professor, Dept. of Eng. and Physics, Univ. of Central Oklahoma,	U.S.A
Mohammed A. HABEEB, Professor, Department of Physics, Faculty of Science, Nahrain University, Baghdad,	IRAQ
Morshed KHANDAKER, Associate Professor, Dept. of Engineering and Physics, Univ. of Central Oklahoma,	U.S.A
Muhammad A. HUSSAIN, Assistant Professor, Dept. of Laser and Optoelectronics Eng., Nahrain University,	IRAQ
Mutaz S. ABDUL-WAHAB, Assistant Professor, Dept. of Electric Engineering, University of Technology,	IRAQ
Nadir F. HABOUBI, Professor, Department of Physics, College of Education, Mustansiriya Univ., Baghdad,	IRAQ
Qian Wei Chang, Professor, Faculty of Science and Engineering, University of Alberta, Edmonton, Alberta,	CANADA
Sebastian ARAUJO, Professor, School of Applied Sciences, National University of Lujan, Buenos Aires,	ARGENTINA
Shivaji H. PAWAR, Professor, D.Y. Patil University, Kasaba Bawada, Kolhapur-416 006, Maharashtra,	INDIA
Xueming LIU, Professor, Department of Electronic Eng., Tsinghua University, Shuang Qing Lu, Beijing,	CHINA
Yanko SAROV, Assistant Professor, Micro- and Nanoelectronic Systems, Technical University Ilmenau,	GERMANY
Yushihiro TAGUCHI, Professor, Dept. of Physics, Chuo University, Higashinakano Hachioji-shi, Tokyo,	JAPAN

SPONSORED AND PUBLISHED BY
THE IRAQI SOCIETY FOR ALTERNATIVE AND RENEWABLE ENERGY SOURCES & TECHNIQUES (I.S.A.R.E.S.T.)

IRAQI JOURNAL OF APPLIED PHYSICS

ISSN (Print): 1813-2065, ISSN (Online): 2309-1673, ISSN (Letters): 1999-656X

Indexed by Scopus 2021

INSTRUCTIONS TO AUTHORS

CONTRIBUTIONS

Contributions to be published in this journal should be original research works, i.e., those not already published or submitted for publication elsewhere, individual papers or letters to editor.

Manuscripts should be submitted to the editor at the mailing address:

Iraqi Journal of Applied Physics, Editorial Board, P. O. Box 55259, Baghdad 12001, IRAQ
Website: www.iraqiphysicsjournal.com
Email: editor@iraqiphysicsjournal.com, editor_ijap@yahoo.co.uk, ijap.editor@gmail.com

MANUSCRIPTS

Two hard copies with soft copy on a compact disc (CD) should be submitted to Editor in the following configuration:

- **One-column** Double-spaced one-side A4 size with 2.5 cm margins of all sides
- Times New Roman font (16pt bold for title, 14pt bold for names, 12pt bold for headings, 12pt regular for text)
- Letters should not exceed 10 pages, papers should not exceed 20 pages and reviews are up to author.
- Manuscripts presented in English only are accepted.
- English abstract not exceed 150 words
- 4 keywords (at least) should be maintained on (PACS preferred)
- Author(s) should express all quantities in SI units
- Equations should be written in equation form (*italic* and symbolic)
- Figures and Tables should be separated from text
- Figures and diagrams can be submitted in colors for assessment and they will be returned to authors after provide printable copies
- Charts should be indicated by the software used for
- Only original or high-resolution scanner photos are accepted
- For electronic submission, articles should be formatted with MS-Word software.

AUTHOR NAMES AND AFFILIATIONS

It is IJAP policy that all those who have participated significantly in the technical aspects of a paper be recognized as co-authors or cited in the acknowledgments. In the case of a paper with more than one author, correspondence concerning the paper will be sent to the first author unless staff is advised otherwise.

Author name should consist of first name, middle initial, last name. The author affiliation should consist of the following, as applicable, in the order noted:

- Company or college (with department name or company division), Postal address, City, state, zip code, Country name, contacting telephone, and e-mail

REFERENCES

The references should be brought at the end of the article, and numbered in the order of their appearance in the paper. The reference list should be cited in accordance with the following examples:

[1] X. Ning and M.R. Lovell, "On the Sliding Friction Characteristics of Unidirectional Continuous FRP Composites", *ASME J. Tribol.*, 124(1) (2002) 5-13.
[2] M. Barnes, "Stresses in Solenoids", *J. Appl. Phys.*, 48(5) (2001) 2000–2008.
[3] J. Jones, **"Contact Mechanics"**, Cambridge University Press (Cambridge, UK) (2000), Ch.6, p.56.
[4] Y. Lee, S.A. Korpela and R. Horne, "Structure of Multi-Cellular Natural Convection in a Tall Vertical Annulus", Proc. 7th International Heat Transfer Conference, U. Grigul et al., eds., Hemisphere (Washington DC), 2 (1982) 221–226.
[5] M. Hashish, "Waterjet Technology Development", High Pressure Technology, PVP-Vol. 406 (2000) 135-140.
[6] D.W. Watson, "Thermodynamic Analysis", ASME Paper No. 97-GT-288 (1997).
[7] C.Y. Tung, "Evaporative Heat Transfer in the Contact Line of a Mixture", Ph.D. thesis, Rensselaer Polytechnic Institute, Troy, NY (1982).

PROOFS

Authors will receive proofs of papers and are requested to return one corrected hard copy with a WORD copy on a compact disc (CD). New materials inserted in the original text without Editor’s permission may cause rejection of paper.

COPYRIGHT FORM

Author(s) will be asked to transfer copyrights of the article to the Journal soon after acceptance of it. This will ensure the widest possible dissemination of information.

OFFPRINTS

Authors will receive offprints free of charge and any additional reprints can be ordered.

SUBSCRIPTION AND ORDERS

Annual fees (4 issues per year) of subscription are:

50 US$ for individuals inside Iraq;	**200** US$ for institutions inside Iraq;
100 US$ for individuals abroad;	**300** US$ for institutions abroad.

Fees are reduced by 25% for I.S.A.R.E.S.T. members. Orders of issues can be submitted by contacting the editor-in-chief or editorial office at admin@iraqiphysicsjournal.com, or editor_ijap@yahoo.co.uk to maintain the address of issue delivery and payment way.

IRAQI JOURNAL OF APPLIED PHYSICS
Vol. 18, No. 2, April-June 2022, pp. 3-10

Wei Yao Zhang
Lu Fang Hao
Ming Xiao Ping
Zhao Yang Liu

Department of Chemical Technology and Engineering,
Faculty of Engineering,
Institute of Technical Processes and Industrial Sciences,
Chao Chang Region, CHINA

Performance of Thermally Regenerative Electrochemical Cycles System

In this work, an analytical model for the performance of thermally regenerative electrochemical cycles system is proposed. This model considers the heat transfer irreversibility, external heat leakage and non-ideal regeneration losses. The symmetry of cells is also considered. The proposed model has provided some necessary design and operation criteria of the system for continuous power output. The general characteristics of system performance are determined. The effects of the external heat leakage on the system performance at maximum power output for different conditions are determined and analyzed.

Keywords: Electrochemical system; Heat transfer; Thermal regeneration; Thermodynamics
Received: 15 April 2022; **Revised:** 21 May 2022; **Accepted:** 28 May 2022

1. Introduction

The abundant heat sources and easily accessible are used in various industries such as nuclear power plants, thermal power plants, and renewable energies [1,2]. Thermal energy is categorized into two: primary energy production and abandonment of waste heat with various temperatures [3,4]. As a low-grade waste heat (<100℃) has a low efficiency during the energy conversion process, it was barely used a few decades ago [5]. Thus, research has faced challenges in low- grade heat harvesting. Most of the previous studies were conducted on electronic thermoelectrics [6] and organic Rankine cycles [2,7]. However, there were still disadvantages of low efficiency, complexity, and a high cost [8,9]. There were also studies that reported to recover the energy from the waste heat with a thermally regenerative electrochemical cycle (TREC). TREC demonstrated 40-50% of Carnot efficiency at a high temperature (>500℃), although it was not thoroughly explored due to a poor cycle efficiency at a low temperature (<100℃) [10].

The effective utilization of low-grade thermal energy, which is continuously and abundantly generated by various energy converters, plays an important role in overcoming energy shortage and satisfying ever growing energy demands. It has become a hot research topic in recent decades [11] by enhancing energy utilization efficiency and reducing the consumption of traditional fossil fuels, alleviating environmental contamination and addressing the problem of greenhouse effect. Various feasible technologies, e.g., organic Rankine cycles [12], three heat sources heat transformers [13], semiconductor thermoelectric devices [14], electrochemical thermoelectric devices [15], etc., have been proposed. Unfortunately, among all these low-grade heat harvesting technologies, only a few of them are currently capable of having small enough volume and providing high enough power output and efficiency simultaneously.

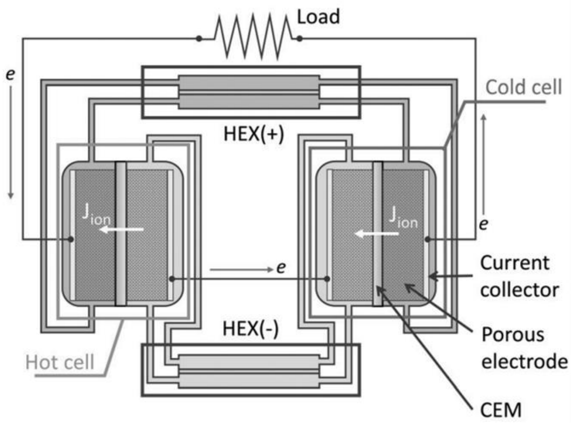

Fig. (1) Schematic diagram of a practical thermally regenerative electrochemical cycle

Recently, by adopting highly reversible electrode materials, a novel thermally regenerative electrochemical cycle (TREC) system based on thermogalvanic effect has been proposed [16]. Due to its high conversion efficiency and small volume, it is regarded as a promising approach to exploit the low-grade thermal energy and draws widely attention. Yang et al. presented a charging-free TREC system [17] and a membrane-free TREC system [18] in succession, which enriched the application scenario of the TREC system. A TREC system was proposed [19] by adopting supercapacitors, which may operate between a wider range of temperature differences. Long et al. investigated the performance of TREC and thermally regenerative electrochemical refrigerator (TRER) systems [20], respectively, by adopting finite time thermodynamics [21] and introducing various objective functions [22]. The influences of the internal resistance, specific heat capacity, specific charge capacity, and isothermal coefficient on the performance of TREC and TRER systems were discussed. In order to generate continuous and high enough power output, an electrochemical system consisting of multiple thermally regenerative electrochemical cycles (TRECs) was presented [23] and discussed its performance characteristics under different operating situations. Moreover, various hybrid systems consisting of TREC and fuel cell [24], TRECs and fuel cell [25], and TRER and solar cell [26] have been proposed, respectively, in order to achieve better performance and higher energy conversion efficiency, which greatly extended the scope of the applications of these systems.

However, it should be pointed out that the irreversibilities of heat transfer [27] between two heat sources and the cells are neglected. As a consequence, there is no restriction of electric current, heat transfer coefficients, and regeneration efficiency for a TRECs system to achieve continuous power output. In other words, the TRECs system is assumed to be capable of realizing the continuous power output if only $(n/m)\geq2$, where n is the total number of the cells adopted in the TRECs system and m indicates the number of the cells charged/discharged at the same time, which is a result that may not coincide with a practical case. Besides, the external heat leakage loss, which has been proved to be important to the performance of traditional thermodynamic cycle [28] and related thermodynamic device [29], was not taken into account because the TREC system cannot generate work at the whole cycle time and the heat transfer coefficients between cells and two heat sources are assumed to be infinite. In addition, the symmetry of the cells inside the TRECs system was not taken into account as well, which is necessary for a practical thermally regenerative electrochemical cycles system operated at steady state.

In the present paper, a TRECs system with continuous power output is established. The heat transfer irreversibility between two heat sources and the cells is considered and the non-ideal regeneration and external heat leakage losses are included. Besides, the symmetry of cells, which is a necessary ingredient for the operation of TRECs system at steady state in practice, is taken into account. With the help of the proposed model, the design and operation criteria of the TRECs system for achieving continuous power output are first deduced. Then, the influences of the external heat leakage are investigated and the general performance characteristics of the TRECs system are reported. In addition, the optimally operating regions of several parameters are determined. Finally, the upper and lower bounds of efficiency at maximum power output are discussed.

2. Proposed Model of TREC system

In a TREC system, copper hexacyanoferrate (CuHCF) with negative temperature coefficient and copper/cupric (Cu/Cu^{2+}) with positive temperature coefficient are chosen as the active materials of positive and negative electrodes in the thermogalvanic cell, respectively, due to their low heat capacity, high charge capacity, and high absolute value of temperature coefficient. Besides, sodium nitrate ($NaNO_3$) and cupric nitrate ($Cu(NO_3)_2$) are, respectively, adopted as the aqueous solutions of positive and negative electrodes, which are separated by an anion membrane. When such a TREC system works as a heat engine, the thermogalvanic cell goes through four processes to fulfill a cycle, which includes two isobaric processes and two isothermal processes, as shown in Fig. (2). During process 1-2, the cell is heated from T_c to T_h under the open circuit condition. In process 2-3, the cell is connected with a power source and charged at constant temperature T_h by contacting the high-temperature heat source. As a consequence, the entropy of the cell increases by absorbing heat from the high-temperature heat source during the electrochemical reaction.

After being charged, the cell is then disconnected from the power source and cooled down from T_h to T_c at the open circuit condition in process 3-4. In the final process i.e., process 4-1, the cell is discharged at constant temperature T_c by connecting with external load and contacting the low-temperature heat source, and the entropy of the cell decreases by releasing heat into the low-temperature heat source during the electrochemical reaction. Besides, in Fig. (2), Q_r denotes the regeneration heat, T_h' and T_c' are the temperatures of the cell in two isobaric processes after regeneration. T_h' and T_c' are different from T_h and T_c due to the non-ideal regeneration.

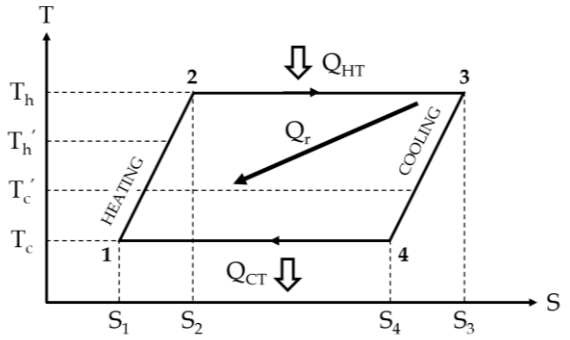

Fig. (2) The T-S diagram of a multiple thermally regenerative electrochemical cycle (TREC) system

It is worthy to point out that geothermal, the waste heat from heat engine, fuel cell, solar cell, and so on can be adopted as the high-temperature heat source of the TREC system. Besides, it should be mentioned that the temperature of the low-grade heat source is variable when the low-grade heat harvesting system is working in transient-state condition. However, when the low-grade heat harvesting system is working in steady-state condition, the waste heat flux generated by different thermodynamic devices such as heat engine, fuel cell, solar cell, and so on, should equal the heat flux extracted by the low-grade heat harvesting system. Therefore, the temperature of the low-grade heat source is constant at steady-state operation. The investigation of the performance characteristics of the low-grade heat harvesting system working in transient-state is complicated. In present paper, the performance characteristics of the TRECs system are investigated under steady-state condition only. This methodology has been adopted by numerous researchers in the researches of various low-grade heat harvesting systems, e.g., TRECs system [25], thermoelectric device [30], thermionic devices [31], absorption refrigerator system [32], organic Rankine cycle [33].

After these four processes, the cell goes back to its initial state, while part of the thermal energy absorbed from the high-temperature heat source is converted into work output resulting from the higher voltage in the discharging process than in the charging process [34,35].

In order to establish a more practical TREC system with continuous power output, a TRECs system consisting of *n* identically thermogalvanic cells which are separated into *n/m* identical cell packs, where *m* denotes the number of the cells included in one cell pack is considered. The cells inside one cell pack go through different processes in a cycle simultaneously [36]. The irreversible TRECs system, as shown in Fig. (3), operates between two heat sources with temperatures T_H and T_C, where Q_{HT} and Q_{CT} are, respectively, the heats absorbed from the high-temperature heat source and released into the low-temperature heat source by the cell packs during the two isothermal processes in a cycle; T_h and T_c are, respectively, the temperatures of the cells in two isothermal processes; Q_r is the regeneration heat transferred between the cells in process 1-2 and process 3-4; Q_{Ha} and Q_{Ca} are the additional heats exchanged between the cell packs and the two thermal sources in the processes 1-2 and 3-4 due to the non-ideal regeneration in a cycle; and Q_L is the external heat leakage between the two thermal sources in a cycle [37]. Note in Fig. (3) that T_h and T_c are different from the temperatures of two thermal sources, namely, T_H and T_C, due to the finite-time heat transfer.

In a TRECs system, the net heat fluxes between the two thermal sources and the charged and discharged cell packs during two isothermal processes can be expressed, respectively, as [23]

$$q_{Hm} = \frac{Q_{Hm}}{t_{ch}} = m(\alpha_c T_h I_{ch} - I_{ch}^2 R) \qquad (1)$$

and

$$q_{Cm} = \frac{Q_{Cm}}{t_{dis}} = m(\alpha_c T_c I_{dis} - I_{dis}^2 R) \qquad (2)$$

where Q_{Hm} and Q_{Cm} are the corresponding absorbed and released net heats by one cell pack, α_c is the temperature coefficient; $I_{ch}^2 R(t_{ch})$ and $I_{dis}^2 R(t_{dis})$ are the Joule heats of one cell released into the high-temperature and low-temperature sources during two isothermal processes, respectively; I_{ch} and I_{dis} denote the charging and discharging electric currents of one cell; t_{ch} and t_{dis} indicate the time durations of charging and discharging processes, and R stands for the internal resistance of one cell

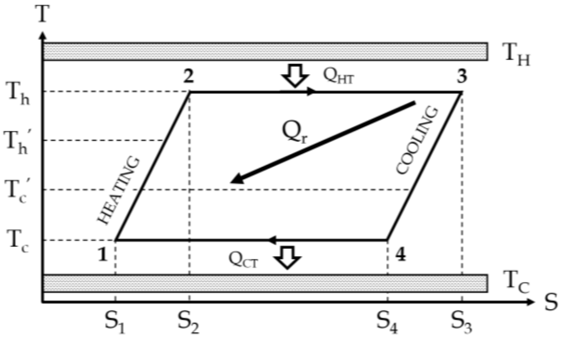

Fig. (3) The T-S diagram of a multiple thermally regenerative electrochemical cycle (TREC) system

By assuming that the heat transfers between heat sources and cells obey linear heat transfer law, q_{Hm} and q_{Cm} can also be expressed as

$$q_{Hm} = mK_H(T_H - T_h) \qquad (3)$$

and

$$q_{Cm} = mK_C(T_c - T_C), \qquad (4)$$

where K_H and K_C are the heat transfer coefficients between cells and heat sources during the two isothermal processes. Using Eqs. (1)-(4), one can obtain the expressions of T_h and T_c as

$$T_h = \frac{I_{ch}^2 R + K_H T_H}{\alpha_c I_{ch} + K_H} \qquad (5)$$

and

$$T_c = \frac{I_{dis}^2 R + K_C T_C}{K_C - \alpha_c I_{dis}}. \qquad (6)$$

It is a good approximation to assume $I_{ch}=I_{dis}=I$, $t_{ch}=t_{dis}=t$, $C_{q,ch}=C_{q,dis}=C_q$, and $K_H=K_C=K_{ht}$. Therefore, the temperature difference of the cells in two isothermal processes can be expressed as

$$\Delta T = T_h - T_c \qquad (7a)$$

$$\Delta T = \frac{K_{ht}^2(T_H - T_C) - \alpha_c I K_{ht}(T_H + T_C) - 2I^3 R\alpha_c}{K_{ht}^2 - \alpha_c^2 I^2} \qquad (7b)$$

It is well known that the regenerator plays an important role in improving the efficiency of a TRECs system. However, the perfect regeneration requires infinite regeneration time i.e., $t_r \rightarrow \infty$, which is unachievable for a practical system. Consequently, the regenerative efficiency can be defined as [23]

$$\eta_r = \frac{2t_r}{\tau} \qquad (8)$$

where $\tau=2t+2t_p$ is the whole cycle time of the TRECs system, $2t_p=2t_r+t_{a12}+t_{a34}$ is the time spent in two isobaric processes, t_{a12} and t_{a34} are, respectively, the additional times in two isobaric processes due to non-ideal regeneration and finite-time heat transfer. The temperatures of the cells in two isobaric processes after regeneration can be expressed as

$$T_h' = T_c + (T_h - T_c)\eta_r \qquad (9)$$

and

$$T_c^{'} = T_h - (T_h - T_c)\eta_r, \tag{10}$$

respectively. To achieve the objective temperatures, i.e., T_h and T_c, after non-ideal regeneration the cells in process 1-2 should absorb heat from the high-temperature source and the cells in process 3-4 should release heat into the low-temperature source. By using Eqs. (9) and (10), the additional heats exchanged between one cell pack and two thermal sources due to the non-ideal regeneration in two isobaric processes can be expressed as

$$Q_{Ham} = mC_p(T_h - T_h^{'}) = m(1-\eta_r)C_p(T_h - T_c) \tag{11}$$

and

$$Q_{Cam} = mC_p(T_c^{'} - T_c) = m(1-\eta_r)C_p(T_h - T_c) \tag{12}$$

respectively, where C_p is the heat capacity of one cell. In order to obtain the relationship between t_{a12}, t_{a34}, and τ, it is rational to introduce logarithmic mean temperature differences in the exchanging heat processes between the cell pack and two thermal sources along paths 1-2 and 3-4. By doing so, Q_{Ham} and Q_{Cam} can also be expressed as

$$Q_{Ham} = mK_{ht}t_{a12}\Delta T_{LM,a12} \tag{13}$$

and

$$Q_{Cam} = mK_{ht}t_{a34}\Delta T_{LM,a34} \tag{14}$$

where

$$\Delta T_{LM,a12} = \frac{\Delta T_{max,a12} - \Delta T_{min,a12}}{Ln\frac{\Delta T_{max,a12}}{\Delta T_{min,a12}}} \tag{15a}$$

$$\Delta T_{LM,a12} = \frac{(T_h - T_c)(1-\eta_r)}{Ln\frac{T_H - T_h\eta_r - T_c(1-\eta_r)}{T_H - T_h}} \tag{15b}$$

and

$$\Delta T_{LM,a34} = \frac{\Delta T_{max,a34} - \Delta T_{min,a34}}{Ln\frac{\Delta T_{max,a34}}{\Delta T_{min,a34}}} \tag{16a}$$

$$\Delta T_{LM,a12} = \frac{(T_h - T_c)(1-\eta_r)}{Ln\frac{T_h - (T_h - T_c)\eta_r - T_c}{T_c - T_C}} \tag{16b}$$

are, respectively, the corresponding logarithmic mean temperature differences [38], $\Delta T_{max,a12}=T_H-T_h{'}$, $\Delta T_{min,a12}=T_H-T_h$, $\Delta T_{max,a34}=T_c{'}-T_C$, and $\Delta T_{min,a34}=T_c-T_C$,. It should be pointed out that the additional times in two isobaric processes are different from each other usually, i.e., $t_{a12} \neq t_{a34}$ because of $T_H-T_h \neq T_c-T_C$, which can be realized from Eqs. (13)-(16). Nevertheless, in order to keep the stable power output of the TRECs system, the cells in one isobaric process attaining the objective temperature, i.e., T_h or T_c, firstly cannot proceed the next process (isothermal process) until the corresponding cells in the other isobaric process attain their objective temperature, i.e., T_c or T_h. Consequently, the additional times in process 1-2 and process 3-4 have the same value t_a which equals the longer additional time in process 1-2 and process 3-4, namely,

$$t_a = \begin{cases} t_{a12}, & T_H - T_h < T_c - T_C \\ t_{a34}, & T_H - T_h > T_c - T_C \end{cases} \tag{17}$$

In addition, by considering that all cells in the TRECs system are equivalent, the relation between t and τ under continuous power output can be deduced as [23]

$$\frac{m}{n} = \frac{t}{\tau} \tag{18}$$

By using Eq. (18), the relation between t_p and t under continuous power output can be further obtained as

$$t_p = \frac{n-2m}{2m}t \tag{19}$$

Substituting Eqs. (17)-(19) into Eq. (8), the regenerative efficiency can be further expressed as

$$\eta_r = 1 - \frac{2m}{n} - \frac{2t_a}{\tau} \tag{20}$$

Using Eqs. (11)-(18), (20), and the relation $C_p=It$, one has

$$\frac{K_{ht}t_a}{C_p} = \frac{c_q}{c_p}\frac{K_{ht}}{I}\frac{n}{m}\frac{t_a}{\tau} \tag{21a}$$

$$M_1 = 1 - \frac{2m}{n} - \frac{2t_a}{\tau} \tag{21b}$$

$$N_1 = \frac{T_c\left(\frac{2m}{n} + \frac{2t_a}{\tau}\right)}{T_H - T_h} \tag{21c}$$

$$M_2 = \frac{T_h\left(\frac{2m}{n} + \frac{2t_a}{\tau}\right)}{T_c - T_C} \tag{21d}$$

$$N_2 = \frac{T_c\left(1 - \frac{2m}{n} - \frac{2t_a}{\tau}\right) - T_C}{T_c - T_C} \tag{21e}$$

$$\frac{K_{ht}t_a}{C_p} = Ln[M_1 - N_1],\ T_H - T_h < T_c - T_C \tag{21f}$$

$$\frac{K_{ht}t_a}{C_p} = Ln[M_2 + N_2],\ T_H - T_h > T_c - T_C \tag{21g}$$

where c_q and c_p are respectively the specific charge capacity and specific heat capacity of the cell, from which the value of t_a/τ can be obtained for given values of m, n, I, K_{ht}, T_H and T_C, by numerical calculation.

In order to make the model of the TRECs system more practical, the external heat leakage loss will be introduced. According to the above analyses and considering the external heat leakage, the net heat absorbed from high-temperature heat source and released into low-temperature heat source in a cycle can be obtained as

$$Q_H = Q_{HT} + Q_{Ha} + Q_L \tag{22a}$$

$$Q_H = \frac{n}{m}(Q_{Hm} + Q_{Ham}) + Q_L \tag{22b}$$

and

$$Q_C = Q_{CT} + Q_{Ca} + Q_L \tag{23a}$$

$$Q_H = \frac{n}{m}(Q_{Cm} + Q_{Cam}) + Q_L \tag{23b}$$

where $Q_L=q_L\tau=K_L(T_H-T_C)\tau$ is the external heat leakage in a cycle, q_L is the corresponding external heat leakage rate, and K_L is the associated heat leakage coefficient. In the present paper, the TRECs system is assumed to be operated only at steady state. Therefore, the corresponding heat fluxes can be expressed as

$$q_H = \frac{Q_H}{\tau} \tag{24}$$

and

$$q_C = \frac{Q_C}{\tau} \tag{25}$$

Using Eqs. (24) and (25), one can obtain the power output (P) and efficiency (η) of the TRECs system as

$$P = q_H - q_C \tag{26}$$

and

$$\eta = \frac{P}{q_H} = \frac{q_H - q_C}{q_H} = 1 - \frac{q_C}{q_H} \qquad (27)$$

A special case, in which the TRECs system is working without adopting a regenerator, will be considered. At this situation, all the heat required in process 1-2 should be absorbed form high-temperature heat source and all the heat in process 3-4 should be released into low-temperature heat source. Meanwhile, the time durations required in process 1-2 and process 3-4 are minimal at this situation. The minimal time duration of the isobaric process can be obtained from Eq. (21) by setting η_r=0, i.e.,

$$M_3 = Ln \frac{T_H - \frac{I^2R + K_{ht}T_C}{K_{ht} - \alpha_C I}}{T_H - \frac{I^2R + K_{ht}T_H}{K_{ht} + \alpha_C I}} \qquad (28a)$$

$$N_3 = Ln \frac{\frac{I^2R + K_{ht}T_H}{K_{ht} + \alpha_C I} - T_C}{\frac{I^2R + K_{ht}T_C}{K_{ht} - \alpha_C I} - T_C} \qquad (28b)$$

$$t_{p,min} = t_a = \begin{cases} \frac{c_p}{c_q}\frac{I}{K_{ht}} t M_3 & T_H - T_h < T_c - T_C \\ \frac{c_p}{c_q}\frac{I}{K_{ht}} t N_3 & T_H - T_h > T_c - T_C \end{cases} \qquad (28c)$$

3. Results and Discussion

The behaviors of t_a/τ and η_r against n are shown in Fig. (4) by using Eqs. (20) and (21). It can be found that t_a/τ decreases with the increase of n monotonically and η_r increases with the increase of n monotonically for given values of m, I and K_{ht}, which can be explained as follow. For a given value m, with the increase of the number of cells adopted in the system, i.e., n, the ratio of the time duration for charging/discharging process to the whole cycle time declines. Therefore, more time can be assigned to the regeneration process. Consequently, higher regeneration efficiency can be achieved and less additional time is required.

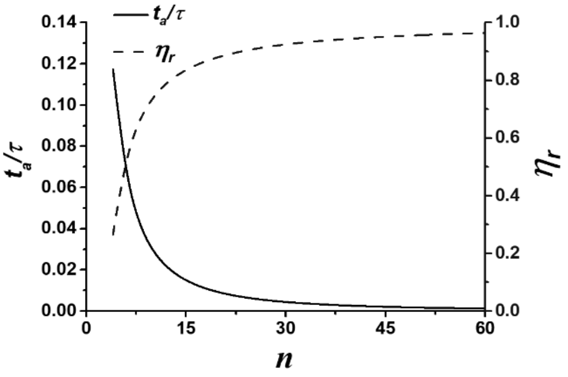

Fig. (4) Curves of t_a/τ and η_r varying with n, where m=1, T_H=333K, T_C=283K, K_{ht}=0.1W/K, I=1ANote that only even integers are physically acceptable values of n

Using Eqs. (21), (24)-(27), one can plot the η-I and P-I curves for different values of K_L, as shown in Fig. (5a) and (4b). It can be seen from Fig. (5) that η decreases monotonically with the increase of I when K_L=0, whereas it is not a monotonic function of I when the external heat leakage is take into account, namely, $K_L \neq 0$. There exists an optimal value $I_{\eta m}$ at which η attains its maximum η_{max} when $K_L \neq 0$. Figure (5) also shows that the power output of the TRECs system is independent of K_L and it is not a monotonic function of I. There exists an optimal value I_{Pm} which makes P attain its maximum P_{max}.

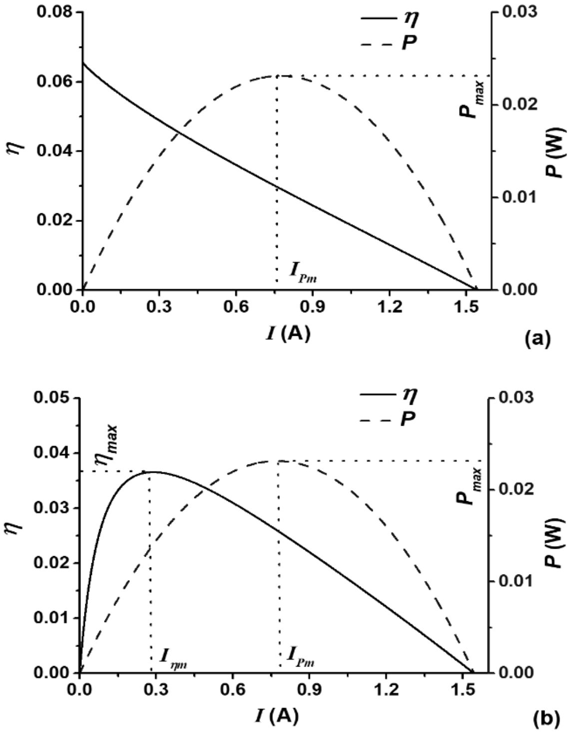

Fig. (5) Variations of η and P with I, where m=1, T_H=333K, T_C=283K, K_{ht}=0.1W/K, (a) K_L=0, (b) K_L=0.02K_{ht}

Using Eqs. (21), (24)-(27), one can also obtain the η-P curves for different values of K_L, as shown in Fig. (6). It can be found that the η-P curve is parabolic when the external heat leakage is negligible. There exists an optimal value η_{Pm} at which the power output of the TRECs system attains its maximum. The power output equals zero when the efficiency of TRECs system attains its maximum. Nevertheless, the η-P curve becomes loop-shaped when $K_L \neq 0$, which means that not only a maximum power output but also a maximum efficiency with finite power output $P_{\eta m}$ exists for the TRECs system.

It can be seen from the solid line in Fig. (6) that when P is smaller than P_{max}, there exist two corresponding efficiencies for a given P, one of which is larger than η_{Pm} and the other of which is smaller than η_{Pm}. In the region of $\eta < \eta_{Pm}$, η increases with the increase of P, which is obviously not optimal. Consequently, the TRECs system without external heat leakage should be operated in the region of $\eta > \eta_{Pm}$, and the corresponding optimal region of electric current can be determined as $I < I_{Pm}$. Similarly, the dashed line in Fig. (6) shows that in the region of $\eta < \eta_{Pm}$ and $P < P_{\eta m}$, P decreases with the decrease of η, which lies beyond the optimally operating region.

As a result, the TRECs system with external heat leakage should be operated in the region of $\eta_{Pm}<\eta<\eta_{max}$ and $P_{Pm}<P<P_{max}$, and the corresponding optimal region of electric current can be determined as $I_{\eta m}<I<I_{Pm}$.

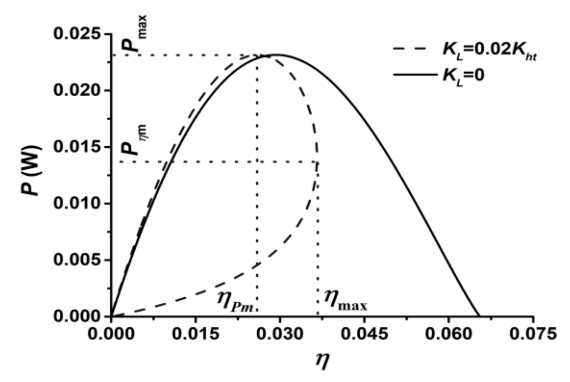

Fig. (6) Curves of *P* varying with *η* for different values of K_L, where *n*=4, *m*=1, T_H=333K, T_C=283K, K_{ht}=0.1W/K

Using Eqs. (21), (24)-(27), one can also generate the *η*-*P* curves for different values of *n* and *m*, as shown in Fig. (7). It can be seen that the performance characteristics of the TRECs system are strongly dependent on the values of both *n* and *m*. More specifically, the maximum power output P_{max} only depends on the value of *m*, whereas the efficiency at maximum power output η_{Pm}, the maximum efficiency η_{max}, and power output at maximum efficiency $P_{\eta m}$ depend on not only the value of *n/m* but also the values of *n* and *m*, which can be realized by comparing the two *η*-*P* curves with the same value of *n/m*, i.e., the solid and dash-dotted curves in Fig. (7). It is worthy to notice that the efficiency only depends on the value of *n/m*.

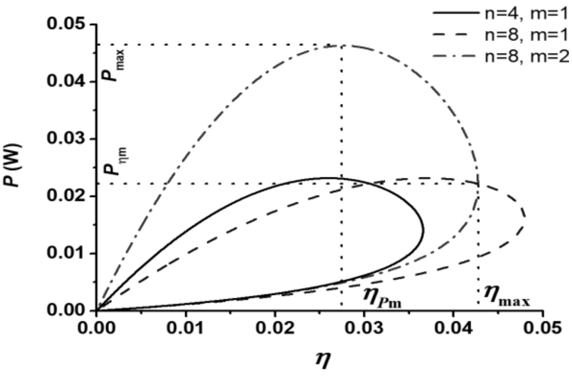

Fig. (7) Curves of *P* varying with *η* for different values of *n* and *m*, where T_H=333K, T_C=283K, K_{ht}=0.1W/K, K_L=0.02K_{ht}

Using Eqs. (21), (24), (25), and (27), one can plot the three-dimensional graph of efficiency varying with *I* and *m* for a given value of *n*, where the values of *m* are selected according to the continuous power output and cells symmetry criteria, i.e., the values of *n/m* are limited as even integers not smaller than 4. The variations of $\eta_{max,n}$ and $m_{\eta m,n}$ with *n* can be further obtained by using Eqs. (21), (24), (25), (27), where $\eta_{max,n}$ is the maximum efficiency for the given value of *n* and $m_{\eta m,n}$ is the corresponding value of *m*. The $\eta_{max,n}$ is not a monotonic function of *n* due to the limitation of *m*. In addition, the relationship between $\eta_{max,n}$ and *n* seems to be chaotic at first sight. However, one can find out that $\eta_{max,n}$ increases with the increase of *n* for a given value of *n/m*, as shown in Fig. (8).

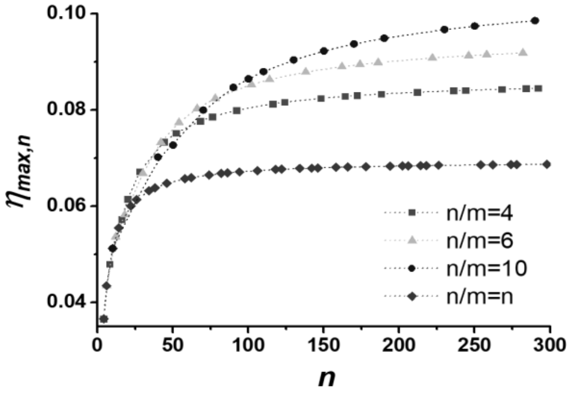

Fig. (8) Variations of $\eta_{max,n}$ with *n* for several given values of *n/m*

Table (1) Values of η_{Pm} or η_{max} of several typical low-grade thermal energy utilization devices

Low-grade thermal energy utilization devices	T_H(K)	T_C(K)	η_{Pm} or η_{max}
Organic Rankine cycle [35]	353	278	η_{max} =7.4%
Semiconductor thermoelectric device [36]	323	283	η_{max} =3.0%
Electrochemical thermoelectric device [37]	338	278	η_{max} =0.25%

4. Conclusion

An analytical model of the TRECs system is proposed for low-grade continuous thermal energy. This model includes the heat transfer irreversibility, external heat leakage loss, and non-ideal regeneration. Using the proposed model and considering the heat transfer irreversibility and non-ideal regeneration, the design and operation criteria of the TRECs system for achieving continuous power output are obtained. Moreover, the values of *n/m* should be limited as even integers to maintain the symmetry of cells during the regeneration process at steady operation is indicated. In addition, the analytic expressions for the efficiency and power output of the TRECs system are derived, by which the influences of the external heat leakage on the performance of the TRECs system are evaluated and the general performance characteristics and optimally operating regions of the TRECs system are revealed. The results obtained from this study may present useful guidance for the optimal design and operation of practical TRECs system with continuous power output.

References

[1] G. Alva, Y. Lin and G. Fang, "An overview of thermal energy storage systems", Energy, 144 (2018) 341–78.

[2] S. Chu and A. Majumdar, "Opportunities and challenges for a sustainable energy future", Nature, 488 (2012) 294–303.

[3] G. Bianchi et al., "Estimating the waste heat recovery in the European Union Industry", Energy Ecol. Environ., 4 (2019) 211-221.

[4] C. Forman et al., "Estimating the global waste heat potential", Ren. Sustain. Energy Rev., 57 (2016) 1568-1579.

[5] C. Haddad et al., "Some efficient solutions to recover low and medium waste heat: Competitiveness of the thermoacoustic technology", Energy Procedia, 50 (2014) 1056-1069.

[6] C. Gao, S.W. Lee and Y. Yang, "Thermally Regenerative Electrochemical Cycle for Low-Grade Heat Harvesting", ACS Energy Lett., 2 (2017) 2326-2334.

[7] J.H. Bahk et al., "Flexible thermoelectric materials and device optimization for wearable energy harvesting", J. Mater. Chem. C, 3 (2015) 10362–10374.

[8] G.J. Snyder and E.S. Toberer, "Complex thermoelectric materials", Nat. Mater., 7 (2008) 105-114.

[9] M. Zebarjadi et al., "Perspectives on thermoelectrics: From fundamentals to device applications", Energy Environ. Sci., 5 (2012) 5147-5162.

[10] S. Quoilin et al., "Techno-economic survey of organic rankine cycle (ORC) systems", Ren. Sustain. Energy Rev., 22 (2013) 168-186.

[11] Y. Huang and Z. Chen, "Performance investigation of an updated alkali metal thermoelectric converter-thermally regenerative electrochemical cycles-thermoelectric generator hybrid system", Energy Conv. Manag., 245 (2021) 114503.

[12] X. Z. and Y.S. Ang, "Conceptual design and performance optimization of a nighttime electrochemical system for electric power generation via radiative cooling", Energy, 242 (2022) 123034.

[13] S. Erzen, E. Açıkkalp and A. Hepbasli, "Performance assessment of a biogas fuelled molten carbonate fuel cell-thermophotovoltaic cell-thermally regenerative electrochemical cycle-absorption refrigerator-alkaline electrolyzer for multigenerational applications", Int. J. Hydrogen Energy, 44(42) (2019) 23741-23749.

[14] X. Tang, G. Li and X. Zhao, "Performance analysis of a novel hybrid electrical generation system using photovoltaic/thermal and thermally regenerative electrochemical cycle", Energy, 232 (2021) 120998.

[15] A. Rajan and S.K. Yee, "System dynamics and metrics of an electrochemical refrigerator based on the Brayton cycle", Cell Rep. Phys. Sci., 3(3) (2022) 100774.

[16] J. Guo et al., "Continuous power output criteria and optimum operation strategies of an upgraded thermally regenerative electrochemical cycles system", Energy Conv. Manag., 180 (2019) 654-664.

[17] A. Abdollahipour and H. Sayyaadi, "A review of thermally regenerative electrochemical systems for power generation and refrigeration applications", Appl. Therm. Eng., 187 (2021) 116576.

[18] R. Chen et al., "A cycle research methodology for thermo-chemical engines: From ideal cycle to case study", Energy, 228 (2021) 120599.

[19] Q. Zhao et al., "Performance evaluation of a novel photovoltaic-electrochemic hybrid system", Energy Conv. Manag., 195 (2019) 1227-1237.

[20] R. Chen et al., "A graphic analysis method of electrochemical systems for low-grade heat harvesting from a perspective of thermodynamic cycles", Energy, 191 (2020) 116547.

[21] X. Zhang et al., "Exploiting the waste heat from an alkaline fuel cell via electrochemical cycles", Energy, 142 (2018) 983-990.

[22] D. Reynard et al., "Efficiency improvement of an all-vanadium redox flow battery by harvesting low-grade heat", J. Power Sources, 390 (2018) 30-37.

[23] Wang Y, Cai L, Peng W, Zhou Y, Chen J. Maximal continuous power output and parametric optimum design of an electrochemical system driven by low-grade heat. Energy Convers. Manage. 2017; 138: 156-61.

[24] H. Fathabadi, "Solar energy harvesting in buildings using a proposed novel electrochemical device as an alternative to PV modules", Ren. Energy, 133 (2019) 118-125.

[25] O.A. Hammadi, "Effects of Extraction Parameters on Particle Size of Titanium Dioxide Nanopowders Prepared by Physical Vapor Deposition Technique", Plasmonics, 15(6) (2020) 1747-1754.

[26] P.A. Linford et al., "Multi-cell thermogalvanic systems for harvesting energy from cyclic temperature changes", J. Power Sources, 399 (2018) 429-435.

[27] D. Huo et al., "Effect of electrolytes on performance of CuHCF electrode of thermally regenerative electrochemical cycle system for harvesting low-grade heat", Energy Conv. Manag., 255 (2022) 115306.

[28] X. Tang, G. Li and X. Zhao, "Effect of air gap on a novel hybrid photovoltaic/thermal and thermally regenerative electrochemical cycle system", Appl. Energy, 293 (2021) 116963.

[29] X. Guo and H. Zhang, “Performance analyses of a combined system consisting of high-temperature polymer electrolyte membrane fuel cells and thermally regenerative electrochemical cycles”, Energy, 193 (2020) 116720.
[30] B. Shapira et al., “Energy extraction and water treatment in one system: The idea of using a desalination battery in a cooling tower”, J. Power Sources, 378 (2018) 146-152.
[31] H. Fathabadi, “Two novel methods for converting the waste heat of PV modules caused by temperature rise into electric power”, Ren. Energy, 142 (2019) 543-551.
[32] K.S. Khashan and O.A. Hamadi, “Features of spot-matrix surface hardening of low-carbon steel using pulsed laser”, Eng. Technol. J., 25 (2007) 168-175.
[33] A.I. Dawahdeh and M.A. Al-Nimr, “Power generation by integrating a thermally regenerative electrochemical cycle (TREC) with a biofuel stove”, Energy, 251 (2022) 123870.
[34] A. Abdollahipour and H. Sayyaadi, “Thermal energy recovery of molten carbonate fuel cells by thermally regenerative electrochemical cycles”, Energy, 227 (2021) 120489.
[35] O.A. Hammadi and N.I. Naji, “Effect of Acidic Environment on the Spectral Properties of Hibiscus sabdariffa Organic Dye used in Dye-Sensitized Solar Cells”, Iraqi J. Appl. Phys., 10(2) (2014) 27-31.
[36] S.-M. Jung et al., “Low-hysteresis manganese hexacyanoferrate (MnHCF) aqueous battery for low-grade thermal energy harvesting”, J. Power Sources, 524 (2022) 231080.
[37] X. Tang et al., “Simulation analysis and experimental validation of enhanced photovoltaic thermal module by harnessing heat”, Appl. Energy, 309 (2022) 118479.
[38] M.A. Al-Nimr, A.I. Dawahdeh and H.A. Ali, “Power generation by integrating a thermally regenerative electrochemical cycle (TREC) with a solar pond and underground heat exchanger”, Ren. Energy, 189 (2022) 663-675.

IRAQI JOURNAL OF APPLIED PHYSICS
Vol. 18, No. 2, April-June 2022, pp. 11-16

Labal Somantiy
Olan Danatua
Ekroma Nadinza

Department of Physical Sciences,
School of natural and Applied Sciences,
Kampala International University,
Kampala, UGANDA

Analytical Study on Effect of Lateral Shear Interferogram on Path Difference in Coherent Optical Systems

In this work, an analytical treatment for the wavefront propagation in optical systems is proposed. This treatment has taken into account the effects of lateral and radial shear interferograms between wavefronts as well as the order of the wavefront that depends on the incidence angle. Results showed that the wavefront ordinary and magnified deviations are convergent at low order rays while the high values of lateral shear can minimize the optical path difference between the propagating wavefronts.

Keywords: Shearing interferometer; Optical system; Interferogram; Path difference
Received: 02 May 2022; **Revised:** 05 June 2022; **Accepted:** 12 June 2022

1. Introduction

In a shearing interferometer, both wavefronts are derived from the system under test, and the interference pattern is produced by shearing one wavefront with respect to the other [1]. Shearing interferometers have the advantage that they do not require a reference surface of the same dimensions as the system under test [2]. In addition, since both the interfering beams traverse very nearly the same optical path, the fringe pattern is less affected by mechanical disturbances [3].

To produce fringes of good visibility with a shearing interferometer, the beams must have adequate spatial coherence [4]. With thermal radiation, this requires a very small illuminated pinhole and, hence, an intense source, usually generating radiation with limited temporal coherence. As a result, much effort went into the design of shearing interferometers which were compensated for white light [5]. With the availability of lasers, which give light with a high degree of spatial and temporal coherence, many simpler arrangements have come into use [6].

The simplest type of shear is a lateral shear. With a nearly plane wavefront, this involves producing two images of the wavefront with a mutual lateral displacement, whereas with a nearly spherical wavefront it requires a similar displacement of the two images of the wavefront over the surface of the reference sphere [7]. Figure (2) shows three typical optical systems which can be used with converging wavefronts. These systems, which are based on the Michelson, Mach–Zehnder, and Sagnac interferometers, were described, respectively [8-10]. A number of modifications of these systems for use with spherical and plane wavefronts have been reviewed [11].

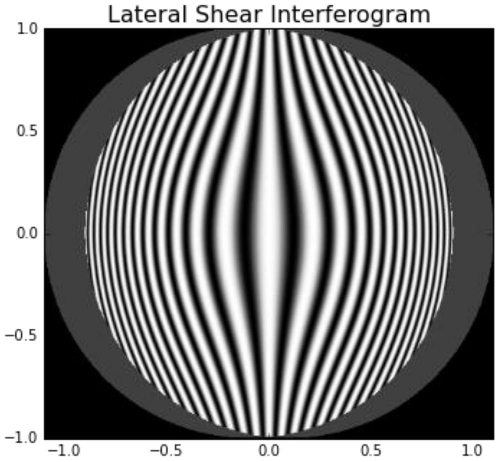

Fig. (1) Shear interferogram with 0.2 shearing

A particularly simple arrangement [12], which can be used with a laser source, consists of a plane-parallel plate. As shown in Fig. (3), the light from the laser is focused by a microscope objective on a pinhole located at the focus of the lens under test. The beam emerging from this lens gives rise to two wavefronts reflected from the front and back surfaces of the plate. The lateral shear between these wavefronts can be varied by tilting the plate and is given by the relation [13]:

$$s = \frac{d\, sin2\theta}{\sqrt{n^2 - sin^2\theta}} \qquad (1)$$

where d is the thickness of the plate and θ is the angle of incidence

A modification of this arrangement [14] uses two separate plates with a variable air gap. This has the advantage that a tilt can be introduced between the two sheared wavefronts to make the interpretation of the fringes easier. The use of a liquid-crystal phase retarder for phase-shifting has been described [15].

A vectorial shearing interferometer based on the Mach–Zehnder configuration, incorporating a pair of wedge prisms, has been described [16]. Variable shear and tilt can be implemented along any direction, permitting the number of fringes and their direction to be controlled.

A possibility that is being explored is the use of a neural network for rapidly identifying and evaluating the primary aberrations in an interferogram [17].

Other forms of shear besides a lateral shear are possible. One is rotational shear in which interference takes place between two images of the test wavefront, one of which is rotated with respect to the other [18,19]. Another is reversal shear [20,21]. Perhaps the most useful is radial shear, in which one of the images of the wavefront is contracted or expanded with respect to the other [22,23].

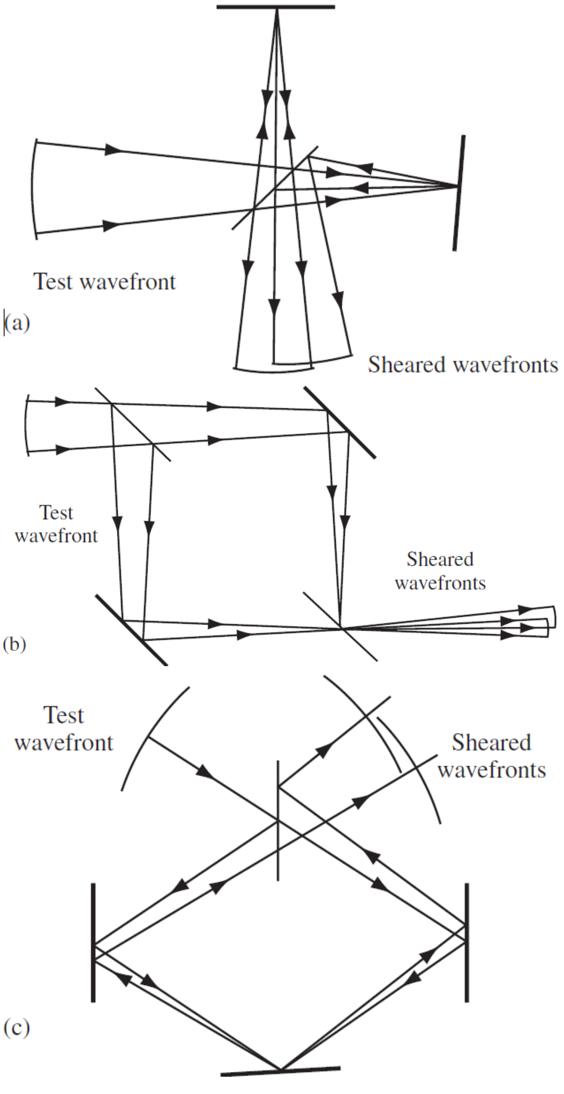

Fig. (2) Lateral shearing interferometers based on (a) the Michelson, (b) the Mach–Zehnder, and (c) the Sagnac interferometers

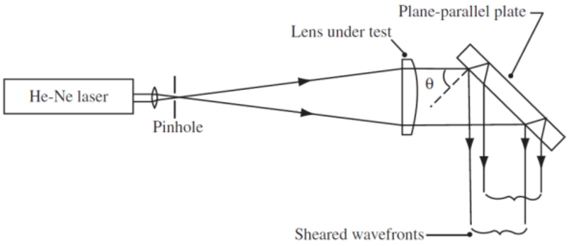

Fig. (3) Lateral shearing interferometer using a laser source and a tilted planeparallel plate [12]

2. Mathematical Treatment

A number of optical arrangements for radial shearing interferometers are available, which have been described [24]. With a thermal light source, a convenient arrangement uses a triangular path (Sagnac) interferometer in which two images of the test wavefront of different sizes are produced by a lens system which is traversed in opposite directions by the two beams [25]. With a laser source, a simple system can be used, consisting of a thick lens [26]. In this arrangement, interference takes place between the directly transmitted wavefront and the wavefront which has undergone one reflection at each surface. An even simpler system is shown in Fig. (4), in which interference takes place between the wavefronts reflected from two spherical surfaces [27,28]. A compact, in-line, radial shearing interferometer using a beamsplitting cube has been described [29]; one can also be set up with two zone plates [30,31].

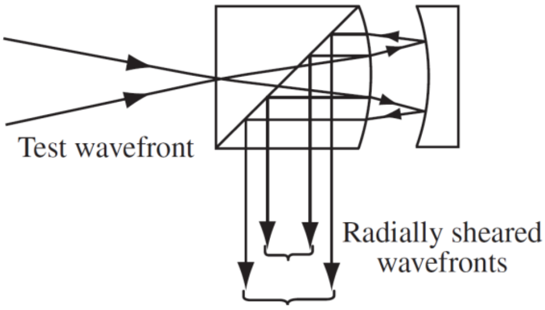

Fig. (4) Schematic diagram of the radial shear interferometer for use with a laser source [28]

To analyze a radial shearing interferogram it is convenient to express the deviations of the wavefront under test from a reference sphere in the form:

$$W(\rho,\theta) = \sum_{n=0}^{k} \sum_{l=0}^{n} \rho^n \left(A_{nl} + B_{nl}\right) \qquad (2)$$

where $A_{nl} = a_{nl}cos^l\theta$ and $B_{nl} = b_{nl}sin^l\theta$, ρ and θ are polar coordinates over a circle of unit radius defining the pupil

If the wavefront with which the test wavefront is compared is magnified by a factor ($1/S$), where $S(<1)$ is known as the shear ratio, the deviations of this magnified wavefront from the same reference sphere are

$$W'(\rho,\theta) = \sum_{n=0}^{k}\sum_{l=0}^{n} S^n\rho^n(A_{nl}+B_{nl}) \qquad (3)$$

Accordingly, the optical path differences in the interferogram are given by the relation

$$p(\rho,\theta) = W(\rho,\theta) - W'(\rho,\theta)$$
$$p(\rho,\theta) = \sum_{n=0}^{k}\sum_{l=0}^{n}(1-S^n)\rho^n(A_{nl}+B_{nl}) (4)$$

3. Results and Discussion

Figure (5) shows the variation of lateral shear of optical wavefront with the incidence angle for different values of order n. It is clear from Fig. (5a) that the fundamental wavefront (n=0) shows higher values of lateral shear and a maximum at the normal incidence (θ=0). The lateral shear is gradually decreasing to reach zero at the incidence angle of 90°. Therefore, the normal incidence is required for the situations of maximum lateral shear in contrast to the most experimental situations (n≥2) where the maximum lateral shear is located around 47°. As the order increases to more than 2, the maximum of lateral shear variation is shifted towards smaller angles. This is in good agreement with literature and published works.

For the case n=1, a completely different behavior is observed for the lateral shear with incidence angle, as shown in Fig. (5b). An apparent maximum is observed at an incidence angle of 38.38°, which makes the order n=1 looks like a singularity or ultra-narrow signal. This behavior is effectively invested in optical design of resonance cavities in laser design.

The interpretation of a lateral shearing interferogram is more difficult than that of an interferogram obtained with a Twyman–Green interferometer, since interference takes place between two aberrated wavefronts instead of between the aberrated wavefront and a perfect reference wavefront. The analysis of such an interferogram has been discussed [32,33]. Apolynomial $\Delta W(x,y)$ is fitted to the measured values of the optical path difference in two interferograms with mutually perpendicular directions of shear; the coefficients of $W(x,y)$ the polynomial representing the errors of the test wavefront, can then be derived from the coefficients of $\Delta W(x,y)$ [34-36]. Other approaches use Fourier filtering [37] or a least-squares method [38-40]. Alternatively, the differences obtained by shearing the test wavefront in a number of directions can be analyzed [41].

In order to introduce the behavior of wavefront deviation W(ρ,θ) as the order is varied, the wavefront deviation was plotted as a function of order (ℓ), as shown in Fig. (6a). Designing the optical system to work at order values smaller than 20 may exhibit low wavefront deviation, which is often required for high-quality optical systems such as single-mode lasers and narrow-band photodetection [42]. Consequently, avoiding the higher values of wavefront deviation is not always an option as some applications of optics may require high wavefront deviation on account of signal quality. Similarly, the wavefront magnified deviation W'(ρ,θ) shows similar behavior with the order n but with reasonably lower amplitude (about two orders of magnitude) as can be seen in Fig. (6b). This similarity can be considered as an advantage for the proposed model especially when being employed in laser design.

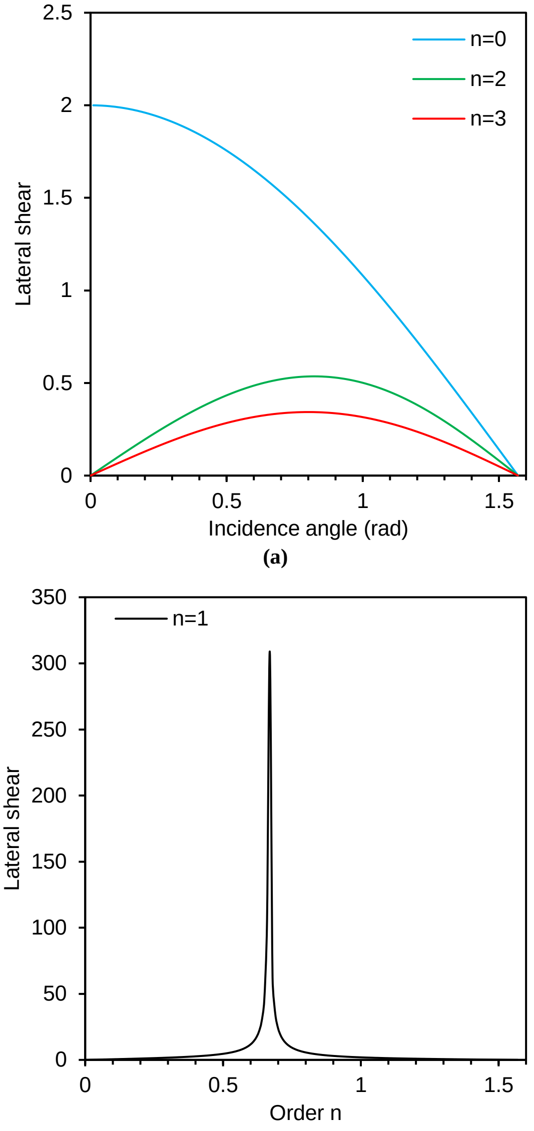

(a)

(b)

Fig. (5) Variation of lateral shear with incidence angle for three different values of order n

The optical path difference (p) can be represented in Fig. (7). It is logical that the behavior of p(ρ,θ) is similar to those of wavefront deviation W(ρ,θ) and wavefront magnified deviation W'(ρ,θ). So, this curve can be used to introduce the effect of lateral shear on the optical design. It is apparent from a comparison of Eq. (4) with Eq. (3) that, with a reasonably small value of the shear ratio ($S<0.5$), the radial shear interferogram is very similar to the interferogram that would be obtained with a

Twyman–Green interferometer, and the wavefront aberrations can be computed in a very similar fashion [43,44].

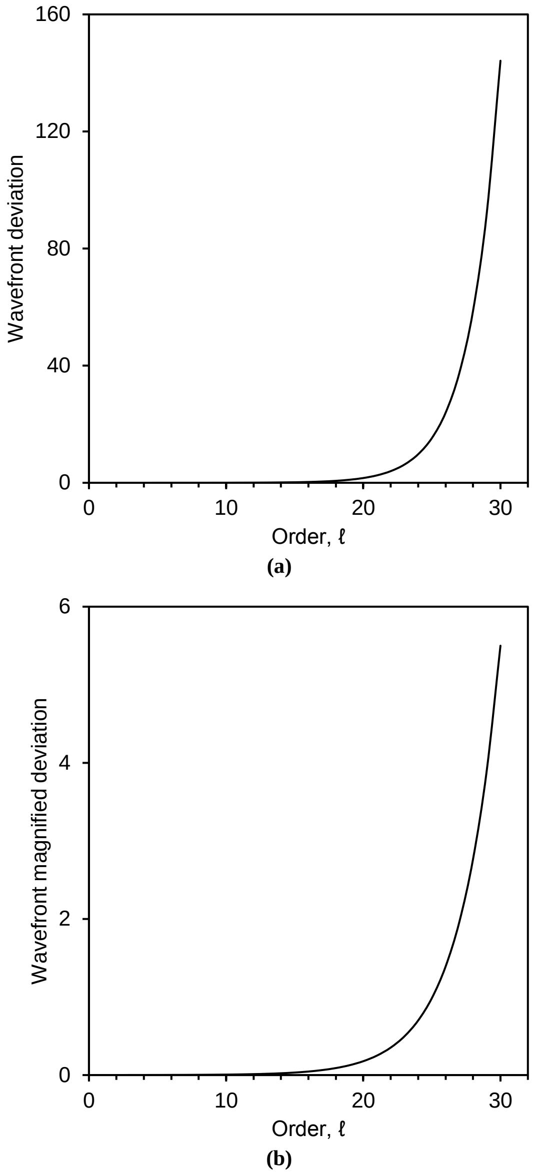

(a)

(b)

Fig. (6) Variation of wavefront deviation (a) and magnified deviation (b) with the order (ℓ) of light rays at incidence angle of 38.38°

The variation of optical path difference p(ρ,θ) with the order ℓ is shown in Fig. (8) for the wavefront deviation W(ρ,θ) and three different cases of the wavefront magnified deviation W'(ρ,θ) (S=0.2, 0.6 and 0.9). The low-order situation is apparently applicable as the optical path difference is ranging with 10^{-6}-10^{-4}. The high-order situation is highly dependent on the value of lateral shear between the propagating wavefronts to reach very low limits at orders of 30. Despite that the practical employments of such situation are rare, they still applicable. Amongst, unstable resonators of high-power lasers are examples.

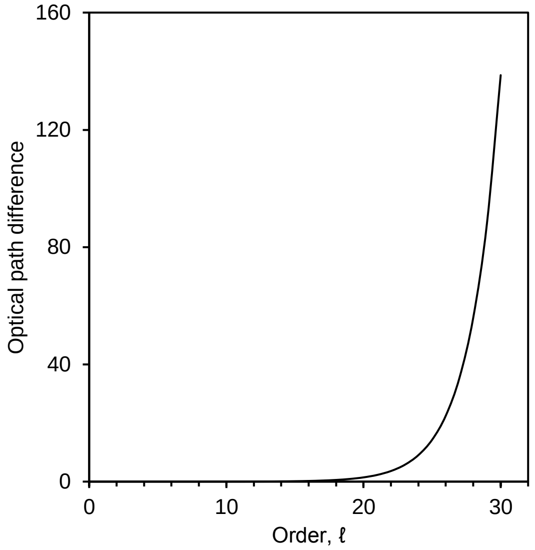

Fig. (7) Variation of optical path difference p(ρ,θ) with the order (ℓ) of light rays at incidence angle of 38.38°

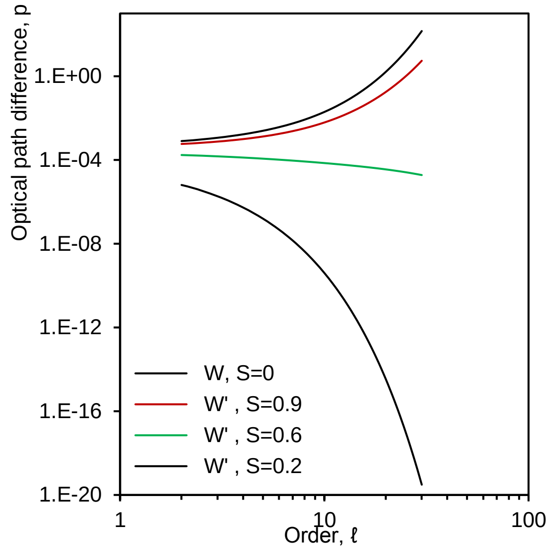

Fig. (8) Variation of optical path difference p(ρ,θ) with the order (ℓ) of light rays at incidence angle of 38.38° for different values of lateral shear s

4. Conclusion

In this work, an analytical treatment for the wavefront propagation in optical systems is proposed. This treatment has taken into account the effects of lateral and radial shear interferograms between wavefronts as well as the order of the wavefront that depends on the incidence angle. Results showed that the wavefront ordinary and magnified deviations are convergent at low order rays while the high values of lateral shear can minimize the optical path difference between the propagating wavefronts. Also, an optimum value of the incidence angle of 38.38° was determined for single-mode propagation, which is highly preferred in the optical systems employed in laser design.

References

[1] G. Xiong et al., “Interference pattern produced by shearing two wavefronts”, J. Opt. Design, 10(5) (2020) 367-372.

[2] Q. Wu et al., “Reference surface for shearing interferometers”, J. Opt. Technol., 13(3) (2017) 101-106.

[3] Y. Tian et al., “Effects of mechanical disturbances on fringe pattern formed by interfering beams”, Opt. Commun., 16(5) (2008) 283-287.

[4] J. Zhang et al., “Production of good-visible fringes with a shearing interferometer for spatial coherence applications”, J. Laser Technol., 9(7) (2008) 451-455.

[5] M.C. Obaiah et al., “Design of shearing interferometers for white light”, Opt. Phys. Lett., 18(1) (2020) 51-54.

[6] K. Bekeruglu et al., “Achievement of high degree of spatial and temporal coherence of laser”, Opt. Optoelect., 5(1) (2005) 89-93.

[7] Z. Li et al., “Image displacement of surface wavefront with reference sphere”, J. Opt. Phot., 10(4) (2020) 417-422.

[8] J. Huang et al., “Optical system with converging wavefronts based on Michelson interferometer”, Opt. Optoelect., 11(7) (2011) 691-698.

[9] A.H. Khan et al., “Optical system with converging wavefronts based on Mach–Zehnder interferometer”, J. Opt. Design, 9(4) (2019) 145-150.

[10] S. Kumar et al., “Optical system with converging wavefronts based on Sagnac interferometer”, J. Opt. Technol., 12(2) (2016) 99-104.

[11] J.H. White et al., “Modifications of optical systems for use with spherical and plane wavefronts”, Opt. Commun., 17(6) (2009) 375-380.

[12] C. Sun et al., “Simple arrangement of interferometer with plane-parallel plate laser source”, J. Laser Technol., 10(8) (2009) 555-560.

[13] O. Girma et al., “Calculation of lateral shear between propagating wavefronts”, Opt. Phys. Lett., 19(2) (2019) 163-168.

[14] H. Garg et al., “A modification of two-plate interferometer with variable air gap”, Opt. Optoelect., 6(2) (2006) 167-172.

[15] N. Ghahramani et al., “Use of liquid-crystal phase retarder for phase-shifting”, J. Opt. Phot., 9(3) (2019) 309-314.

[16] S. Xiang et al., “A vectorial shearing interferometer based on Mach–Zehnder configuration with wedge prisms”, Opt. Optoelect., 12(8) (2012) 725-730.

[17] L. Menini et al., “Using neural network for rapidly identification and evaluation of primary aberrations in interferograms”, J. Opt. Design, 8(1) (2018) 185-190.

[18] P. Kebria et al., “Rotational shear between two test wavefront”, J. Opt. Technol., 14(5) (2018) 305-310.

[19] L. Wang et al., “Analysis of rotational shear interferogram two images”, Opt. Commun., 18(1) (2010) 63-68.

[20] J. Qian et al., “Reversal shear interferometry”, J. Laser Technol., 11(9) (2010) 301-310.

[21] Y. Jiang et al., “Minimization of reversal shear in optical system based on interferometer”, Opt. Phys. Lett., 18(3) (2018) 301-308.

[22] A. Morshed et al., “Radial shear of relatively-moving visible signals”, Opt. Optoelect., 7(3) (2007) 221-226.

[23] A.A. Maciejewski et al., “Effects of radial shear on propagation of co-propagating wavefronts”, Opt. Optoelect., 8(4) (2008) 301-310.

[24] C Anderson et al., “Design considerations of high-efficiency radial shearing interferometer”, J. Opt. Phot., 8(2) (2018) 201-206.

[25] G. Sellis et al., “Arrangement of Sagnac triangular path interferometer with thermal light source”, J. Opt. Design, 7(7) (2017) 589-594.

[26] N. Katsikis et al., “A simple interferometer system using laser source and thick lens”, J. Opt. Technol., 15(9) (2019) 1107-1112.

[27] S. Rakshit et al., “Analysis of interference between wavefronts reflected from two spherical surfaces”, Opt. Commun., 19(4) (2011) 411-418.

[28] M. Kumbasar et al., “Spherical-surface reflection interferometer for propagating wavefronts”, J. Laser Technol., 12(10) (2011) 691-700.

[29] M. Papadopoulos et al., “A compact, in-line, radial shearing interferometer using a beamsplitting cube”, Opt. Phys. Lett., 17(4) (2017) 421-426.

[30] O.A. Hammadi and M.S. Edan, “Temperature Dependencies of Refractive Index and Optical Elasticity Coefficient on Lens Induced in Nd:YAG Crystal”, Iraqi J. Appl. Phys., 8(1) (2012) 35-41.

[31] C. Pan et al., “Two-zone-plates radial shearing interferometer”, J. Opt. Phot., 7(1) (2017) 21-26.

[32] C.-Y. Zu et al., “Analysis of Twyman–Green interferogram between two aberrated wavefronts”, Opt. Optoelect., 10(6) (2010) 553-556.

[33] R. Ghosh et al., “Twyman–Green interferometer of two propagating wavefronts with optical aberration”, J. Opt. Design, 6(4) (2016) 367-372.

[34] E. Recupero et al., “determination of optical path difference in two interferograms with mutually shear perpendicular directions”, J. Opt. Technol., 16(2) (2020) 87-92.

[35] K. Chandra Pati et al., “Numerical analysis of optical path difference of two perpendicular”, Opt. Commun., 20(8) (2012) 805-810.

[36] S. Mukhija et al., “Optical path difference between two interferograms consisting of mutual

perpendicular shear directions", J. Laser Technol., 13(11) (2012) 1543-1550.

[37] U. Vianney et al., "Fourier filtering of optical path difference between two interferograms", Opt. Phys. Lett., 15(6) (2015) 313-320.

[38] A. Sergyienko et al., "Analysis of optical path difference in interferometer using least-squares method", Opt. Phys. Lett., 16(5) (2016) 535-540.

[39] O.A. Hamadi and K.Z. Yahiya, "Optical and electrical properties of selenium-antimony heterojunction formed on silicon substrate", J. Pure Appl. Sci., Univ. Sharjah, 4(2) (2007) 1-11.

[40] D. Carter et al., "Analysis of mutual perpendicular shear directions for propagating wavefronts using least-squares method", J. Opt. Design, 10(6) (2020) 483-488.

[41] R. White et al., "Estimation of optical path difference in two-zone-plates interferogram using least-squares method", J. Opt. Technol., 11(3) (2015) 303-310.

[42] X. Zhang et al., "Multi-directional optical path difference due to shearing wavefront", Opt. Commun., 22(6) (2014) 633-638.

[43] J. Rogers et al., "Radial shear analysis of Twyman–Green free-aberration interferometer", J. Laser Technol., 14(12) (2013) 1-10.

[44] C. Gejdenson et al., "Design considerations of low-aberration Twyman–Green interferometer with radially sheared wavefronts", J. Opt. Phot., 6(12) (2016) 1143-1148.

IRAQI JOURNAL OF APPLIED PHYSICS
Vol. 18, No. 2, April-June 2022, pp. 17-22

Effects of Dual-Magnetron Configuration on Electrical Characteristics of Argon Discharge Plasma

Unal Demraluğlu
Murat Selçan

Department of Electrical and Electronic Engineering, Faculty of Engineering and Natural Sciences, Bahçeşehir University, 34353 Beşiktaş, Istanbul, TURKEY

In this work, the effects of dual magnetron configuration on the electrical characteristics (mainly current-potential) of the argon discharge plasma were presented. These characteristics include the ion and electron currents when ion and electron temperatures are comparable in addition to the ion current when electron temperature is reasonably higher than the ion temperature. Dual magnetrons (i.e., magnetron on each electrode) can efficiently confine the charge carriers (ions and electrons) through the volume from electrode surface towards the center of inter-electrode distance. This effect may extend to the opposite electrode when sufficiently large values of magnetic flux densities are used. Employment of dual magnetron configuration has caused the ion current to increase by 50% while the electron current was increased by 100%.

Keywords: Discharge plasma; Argon discharge; Dual magnetron; Electrical characteristics
Received: 11 April 2022; **Revised:** 13 May 2022; **Accepted:** 20 May 2022

1. Introduction

Magnetron sputtering is a well-established film growth technique as a compromise between atomic level deposition and reasonable deposition rates. Also, deposition at relatively low temperatures is allowed by this technique, therefore, the synthesis of novel structures containing metastable, non-equilibrium phases or of highly oriented materials is valuable feature [1-4]. However, magnetron sputtering is rather complex with many variables affecting the final product and not only the development of new coatings is needed but also the investigation of how the synthesis process affects the final properties of a film is a requirement [5-8].

Glow discharge is low-temperature neutral plasma where the number of electrons is equal to the number of ions despite that local but negligible imbalances may exist at walls [10-12]. Glow discharge is described as self-sustaining plasma, i.e., the avalanche effect of electrons keeps the continuous production of ion species [13,14].

If an initial voltage is applied on a gas sample between two electrodes at sufficient separation, little current will flow through this sample due to the ionization effects in the gas [15,16]. As the applied voltage is increased to reach the breakdown voltage, the energy given to ions is increased too that increases their collisions with atoms and electrodes [17,18]. Accordingly, more ions and electrons are produced due to the ionization and secondary electron emission effects, which lead to increase the flowing current gradually approaching the breakdown point beyond which the avalanche occurs and the current increases drastically in the Townsend discharge region [19,20].

Probes (initially called "sounding electrodes") were first used in the late 19th and early 20th centuries in an attempt to measure the voltage distribution in gas discharges and the most important type of probes is Langmuir probe. Langmuir probes are used in low temperature or cold plasmas [21] (approximately a few electron volts) to measure some parameters of the plasma, such as plasma density, electron temperature, and plasma potential. Typically, Langmuir probe consists of a bare wire or metal disk, which is inserted into plasma and electrically biased with respect to a reference electrode to collect electron and/or positive ion currents [22-24]. The use of a cylindrical (wire) probe in a gas discharge tube is shown in Fig. (1) [20]. The case is a glow discharge plasma into a glass tube (or other evacuated vessel) with pressures between 10^{-2}–10^{2} mbar. The electric discharge is produced by applying a high DC voltage (300-600V or more) and the corresponding discharge current is in the range of 0.1-100 mA [25-28].

Langmuir probe is inserted at one or more locations along the length of the tube, with the exposed tip prominent into the plasma column [29]. The early users of Langmuir probe assumed that the potential of the plasma at the probe location (known as the plasma or space potential) can be determined by measuring the potential on the probe relative to one of the electrodes [30]. However, this procedure determines the floating potential of the probe which is in general not the same as the plasma potential [31]. By definition, an electrically floating probe does not collect net current from the plasma, and thus its potential rises and falls to whatever potential is necessary to maintain zero net current [32-34].

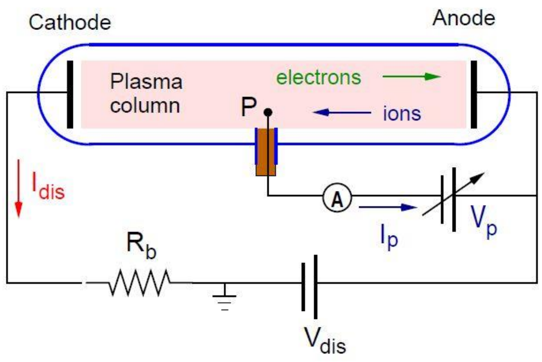

Fig. (1) Schematic diagram of basic gas discharge plasma device at low gas pressure (<1.33 mbar) [35]

Because of the smaller mass of electrons in typical plasma, they have higher thermal velocities than the positive ions even both are at the same temperature [36]. However, electrons usually have higher temperatures than positive ions. Plasma is electrically neutral by definition and electron and ion densities are nearly equal, however, a floating Langmuir probe will tend to draw higher electron current because they reach the probe faster than ions due to difference in mass [37-39]. The probe floats to a negative potential relative to the plasma because the net current to the floating probe must be zero, therefore, further collection of electrons is retarded and ion collection is enhanced [40]. This is why the floating potential is less than that potential of plasma with respect to the walls of the device at a given location in the plasma [41]. Floating potential is generally a few volts positive with respect to the walls because the swifter electrons tend to escape to the walls first, leaving the plasma with a slight excess of positive space charge [42,43].

The bulk of the plasma is "quasineutral" where electron and ion densities are the same, and the potential difference between the bulk of the plasma and the wall is concentrated in a thin layer or sheath near the wall [44]. The gradient of the plasma potential determines the electric field that is responsible for energizing the electrons, which maintain the discharge through ionization [45,46].

Figure (2) shows the typical current-voltage characteristics for Langmuir probe diagnosis of plasma. When the bias voltage (V_B) on the probe is sufficiently negative with respect to the plasma potential (V_P), the probe collects the ion saturation current (I_{is}) and continues to collect positive ions until the bias voltage reaches plasma potential (V_P), at which ions begin to be repelled by the probe. For V_B>>V_P, all positive ions are repelled, and the ion current to the probe vanishes (I_i=0).

For a Maxwellian ion distribution at ion temperature T_i, the dependence of the ion current $I_i(V_B)$ (usually taken to be the negative current) on V_B is given by [47]

$$I_i(V_B) = \begin{cases} I_{is} exp\left[\frac{e(V_P - V_B)}{k_B T_i}\right] & V_B \geq V_P \\ -I_{is} & V_B < V_P \end{cases} \qquad (1)$$

where e is the electron's charge, and k_B is the Boltzmann constant

If ion temperature (T_i) is comparable to electron temperature (T_e), the ion saturation current (I_{is}) is given by [47]

$$I_{is} = \frac{1}{4} e n_i v_{i,th} A_p \qquad (2)$$

where n_i is the ion density, $v_{i,th}=(8k_BT_i/\pi m_i)^{1/2}$ is the ion thermal speed, m_i is the ion mass, and A_p is the probe collecting area [47]

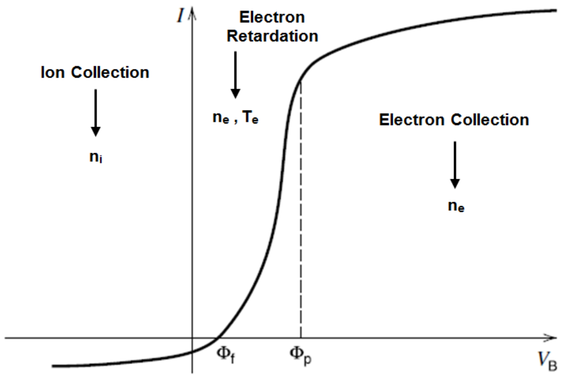

Fig. (2) Typical current-voltage characteristics of Langmuir probe in plasma [48]

If T_e>>T_i, the ion saturation current is not determined by the ion thermal speed, but rather is given by the Bohm ion current [47]

$$I_{is} = I_{Bohm} = 0.6 e n_i \sqrt{\frac{k_B T_e}{m_i}} A_p \qquad (3)$$

The determination of ion current by the electron temperature when T_e>>T_i is a kind of anticipation and the physical reason for the dependence I_{is}~$(k_BT_e/m_i)^{1/2}$ has to do with the formation of a sheath around a negatively biased probe [47]. If an electrode in plasma has a potential different from the local plasma potential, the electrons and ions distribute themselves spatially around the electrode in order to limit, or shield, the effect of this potential on the bulk plasma. A positively biased electrode acquires an electron shielding cloud surrounding it, while a negatively biased electrode acquires a positive space charge cloud. For a negatively biased electrode, the characteristic shielding distance of the potential disturbance is the electron Debye length [49]

$$\lambda_{De} = \left(\frac{\varepsilon_0 k_B T_e}{e^2 n_e}\right)^{1/2} \qquad (4)$$

For V_B>>V_P the probe collects electron saturation current (I_{es}). For V_B<V_P the electrons are partially repelled by the probe, and for a Maxwellian electron velocity distribution, the electron current decreases exponentially with decreasing V. For V_B<<V_P all electrons are repelled, so that I_e=0. The electron current as a function of V_B can be expressed as

$$I_e(V_B) = \begin{cases} I_{es} exp\left[-\frac{e(V_P - V_B)}{k_B T_e}\right] & V_B \leq V_P \\ I_{es} & V_B > V_P \end{cases} \quad (5)$$

The electron saturation current (I_{es}) is given by

$$I_{es} = \frac{1}{4} e n_e v_{e,th} A_p \quad (6)$$

where n_e is the electron density, $v_{e,th} \equiv (8k_B T_e/\pi m_e)^{1/2}$ is the electron thermal speed, and m_e is the electron mass

As can be seen from equations (2), (3) and (6), the electron saturation current will be much greater than the ion saturation current because $n_e = n_i$ and $m_e << m_i$. For example, in an argon discharge plasma where $T_e >> T_i$, according to equations (3) and (6), one can find that [50]

$$\frac{I_{es}}{I_{is}} = \frac{\sqrt{\frac{m_i}{m_e}}}{0.6\sqrt{2\pi}} = \frac{271}{1.5} = 180$$

In this work, the effects of dual magnetron configuration on the electrical characteristics (mainly current-potential) of the argon discharge plasma were presented. These characteristics include the ion and electron currents when ion and electron temperatures are comparable in addition to the ion current when electron temperature is reasonably higher than the ion temperature.

2. Experimental Work

A dc glow discharge plasma system employing the closed-field dual magnetron assembly was used in this work. Electrodes (anode and cathode) were made of stainless steel and each was a disk of 8 cm in diameter and 4 mm in thickness. Two annular concentric magnets were placed behind each electrode to form the magnetron configuration, as shown in Fig. (3). The outer diameters of the two magnets were 8 cm and 4 cm, while the inner diameters were 4 cm and 3.2, respectively. The electrodes were connected to a DC power supply to provide the electrical power required for discharge. The lower electrode (anode) could be move vertically with respect to the fixed upper electrode (cathode) to adjust the separation of the two electrodes from 1 to 10 cm. The results in figures (4), (5) and (6) were obtained at inter-electrode distance of 5 cm.

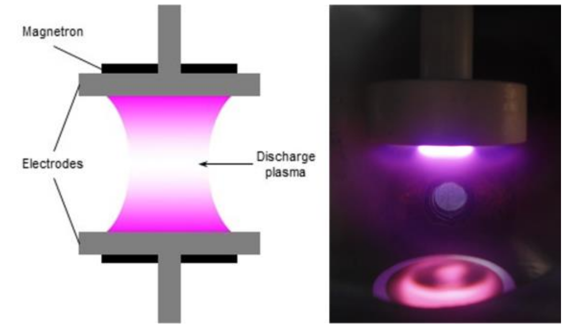

Fig. (3) Schematic diagram (left) and photograph (right) of the dc glow discharge plasma system employing dual magnetron configuration

Pure argon gas was used to produce the discharge plasma, as shown in Fig. (3). A DC power supply up to 5 kV was used for electrical discharge between the electrodes and both breakdown voltage (up to 1 kV) and discharge current (up to 100 mA) were monitored by two digital voltmeter and ammeter, respectively. A current limiting resistor of 6.75 kW was connected in series to the discharge circuit in order to control the current flowing in the circuit. The discharge chamber was evacuated by a two-stage Leybold-Heraeus rotary pump and the vacuum inside chamber was measured by Pirani gauge connected to a vacuum controller from Balzers VWS 120. Argon gas was supplied to the chamber through a fine-controlled needle valve (0-160 ccm) to control the gas pressure inside the chamber.

3. Results and Discussion

Figure (4) shows the variation of ion current with applied potential with and without dual-magnetron assembly under the condition that the ion and electron temperatures are comparable. It is clear that the saturation current in the reverse biasing condition is not affected by the employment of dual-magnetron assembly and maintained at approximately constant value (~0.02μA). In contrast, the ion current in the forward biasing condition shows identical behaviors before and after employing the dual-magnetron assembly. However, the maximum ion current has increased from 166 to 249 μA after this assembly was used. This increase is attributed to the much more efficient confinement resulted from the dual-magnetron configuration.

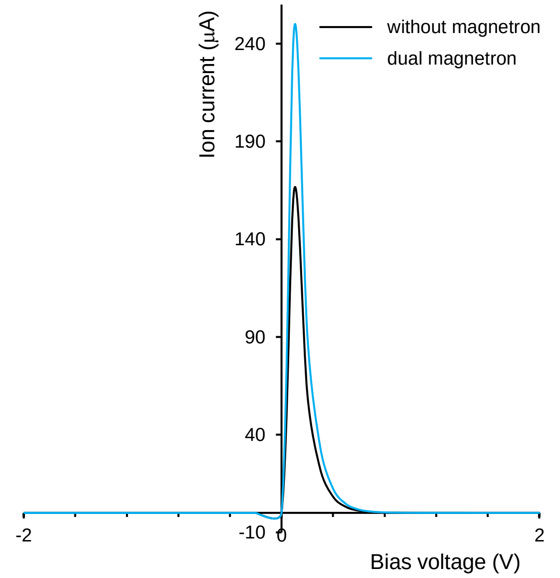

Fig. (4) Variation of ion current with applied potential with and without dual-magnetron assembly under the condition that the ion and electron temperatures are comparable ($T_i \approx T_e$)

Figure (5) shows the variation of ion current with applied potential with and without dual-magnetron assembly under the condition that the electron temperature is reasonably higher than the ion temperature ($T_e >> T_i$). It is also clear that the saturation current in the reverse biasing condition is maintained at approximately constant value (~1nA). In contrast, the ion current in the forward biasing condition shows identical behaviors before and after employing the dual-magnetron assembly. However, the maximum ion current has decreased to 6.7% from its value according to the previous condition. This behavior is obvious due to the reduction in kinetic energy of the ions, so, their contribution to the discharge current is reduced [51].

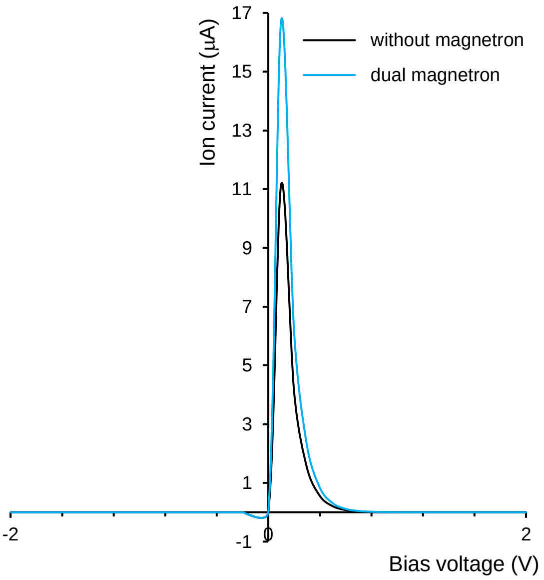

Fig. (5) Variation of ion current with applied potential with and without dual-magnetron assembly under the condition $T_e >> T_i$

Figure (6) shows the variation of electron current with applied potential with and without dual-magnetron assembly under the condition that the ion and electron temperatures are comparable. It is clear that the saturation current in the reverse biasing condition is not affected by the employment of dual-magnetron assembly and maintained at approximately constant value (~25μA). In contrast, the ion current in the forward biasing condition shows identical behaviors before and after employing the dual-magnetron assembly. However, the current after employing this assembly has increased by 100% than the case without this assembly. This increase is attributed to the much more efficient confinement resulted from the dual-magnetron configuration. Also, the electrons are affected by the magnetic confinement much higher than the Ar^+ ions due to their smaller mass.

The application of a weak magnetic field perpendicularly to the cathode surface facilitates the ignition of the discharge and enhances - depending on the operating pressure and the inter-cathode distance - the cathode effect by promoting an increase of the residence time of electrons in the cathodic cavity and by reducing the lateral diffusion. The nature of the gas affects also the discharge properties.

By increasing the inter-cathode distance, the electron temperature decreases, as shown in Fig. (7). At low inter-cathode distances, the electrons lose little energy in inelastic collisions with the atoms/molecules and their mean value of the kinetic energy (electron temperature) is high. As the distance *d* increases, more collisions occur, the electron kinetic energy loss through electron inelastic collisions with neutral atoms/molecules increases thus the electron temperature decreases. Also, because of their high electron affinity, the N_2 atoms capture low energy electrons from plasma and form negative ions with the effects of increasing of temperature of the plasma electrons for low *Pd* values [52].

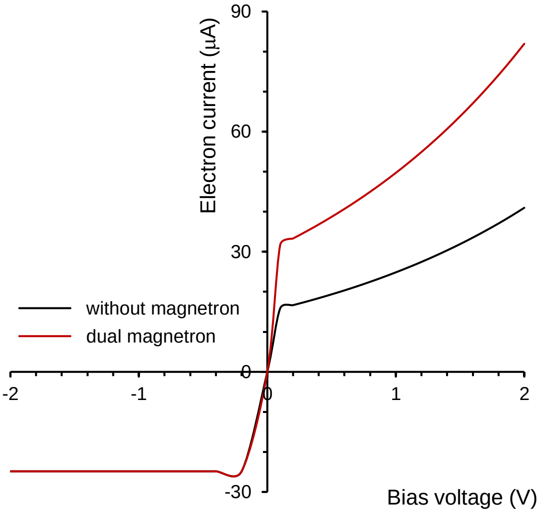

Fig. (6) Variation of electron current with applied potential with and without dual-magnetron assembly under the condition that the ion and electron temperatures are comparable ($T_i \approx T_e$)

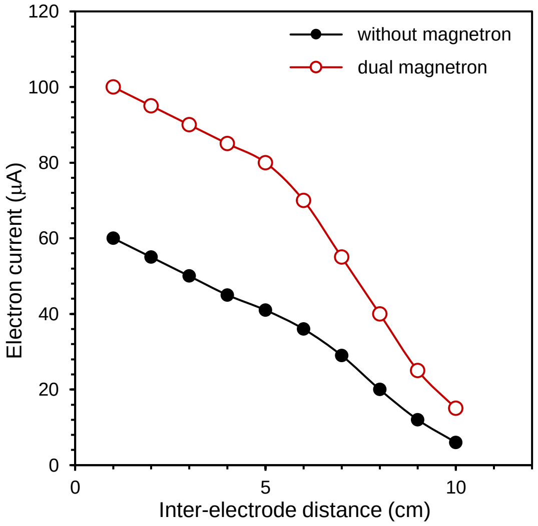

Fig. (7) Variation of electron current with inter-electrode distance with and without dual-magnetron assembly under the condition that the ion and electron temperatures are comparable ($T_i \approx T_e$)

4. Conclusion

In summary, the high quality InN thin films deposited on (100) silicon substrates with the GaN buffer layer is critical to achieve nucleation and duplicate orientation. The InN films are highly oriented in the *c*-axis direction. The GaN buffer layer improved the crystal quality effectively which was smaller surface roughness. The PL results reveal that band gap of InN/gaN structure was about 0.79 eV. Also, the high background-carrier concentration may be caused by a structural defect and/or oxygen incorporation.

References

[1] A. Aijaz, Design and Characterization of a Synchronous Co-axial Double Magnetron Sputtering System, MSc thesis, Department of Physics, Chemistry & Biology, Linköping University, Sweden, p. 10, 38 (2009).
[2] A. Bogaerts et al., “Gas discharge plasmas and their applications (Review)”, Spectrochimica Acta Part B, 57 (2002) 609–658.
[3] A. Bojarov, M. Radmilovic-Radjenovic and Z. Petrovic, Effect of the ion induced secondary electron emission on the characteristics of RF plasmas, Publ. Astron. Obs. Belgrade, 89, 131-134 (2010).
[4] A.A. Solov’ev, Investigation of Plasma Characteristics in an Unbalanced Magnetron Sputtering System, Plasma Phys. Rep., 35(5), 399–408 (2009).
[5] Brown S.C., “Basic data of plasma physics: The fundamental data on electrical discharges in gases,” New York: American Institute of Physics, c1994 pp 142-163, 209-221, 247-254.
[6] C. O’Leary, Design, Construction and Characterisation of a Variable Balance Magnetron Sputtering System, Department of Electronic Engineering, Dublin City University, Ireland, p. 15 (1999).
[7] E. Martines, Electrostatic fluctuations in a direct current magnetron sputtering plasma, Phys. of Plasmas, 8(6), 3042-3050 (2001).
[8] E.F. Kotp and A.A. Al-Ojeery, Studies The Effect Of Magnetic Field On Argon Plasma Characteristics, Australian J. Basic Appl. Sci., 6(3) (2012) 817-825.
[9] E.V. Shun’ko, Langmuir Probe in Theory and Practice (contents and introduction only), Universal Publishers, Boca Raton, Florida, USA (2008).
[10] F. Ghaleb and A. Belasri, Numerical and theoretical calculation of breakdown voltage in the electrical discharge, Radiation Effects and Defects in Solids, 1, 1-7 (2012).
[11] G. Petraconi, Longitudinal Magnetic Field Effect on the Electrical Breakdown in Low Pressure Gases, Brazilian J. of Physics, 34(4B), 1662-1666 (2004).
[12] H. Yasuda, L. Ledernez, F. Olcaytug and G. Urban, Electron dynamics of low-pressure deposition plasma, Pure Appl. Chem, 80(9), 1883-1892 (2008).
[13] H.R. Griem, “Principle of Plasma Spectroscopy,” Cambridge University Press, 1997, p.281
[14] I. Levchenko, Stable plasma configurations in a cylindrical magnetron discharge, Appl. Phys. Lett., 85(12), 2202-2204 (2004).
[15] I. Svadkovski, D. Golosov and S. Zavatskiy, Characterisation parameters for unbalanced magnetron sputtering systems, Vacuum, 68, 283–290 (2003).
[16] J. Goree and T. E. Sheridan, Magnetic field dependence of sputtering magnetron efficiency, Appl. Phys. Lett., 59(9), 1052-1054 (1991).
[17] J. Park et al., “Gas breakdown in an atmospheric pressure radio-frequency capacitive plasma source,” J. Appl. Phys., 89(1) (2001) 15-19.
[18] J.-C. Wang, N. Leoni, H. Birecki, O. Gila and M.J. Kushner, Electron current extraction from radio frequency excited micro-dielectric barrier discharges, J. Appl. Phys., 113 (2013) 033301
[19] J.J. Shi and M.G Kong, “Cathode fall characteristics in a dc atmospheric pressure glow discharge,” J. Appl. Phys., 94(9) (2003) 5504-5513.
[20] J.M. Meek and J.D. Craggs, “Electrical Breakdown of Gases,” Wiley (NY, 1978), 697.
[21] J.-S. Baek and Y.J. Kim, Cooling Effect Enhancement In Magnetron Sputtering System, 5th Inter. Conf. on CFD in the Process Industries CSIRO, Melbourne, Australia 13-15 December 2006, 1-5.
[22] J.W. Bradley, Measurements of the sheath potential in low density plasmas, J. Phys. D: Appl. Phys., 25, 1443-1453 (1992).
[23] K. Sarakinos, J. Alami and S. Konstantinidis, High power pulsed magnetron sputtering: A review on scientific and engineering state of the art, Surf. Coat. Technol., 204, 1661–1684 (2010).
[24] L. Conde, An introduction to Langmuir probe diagnostics of plasmas, Departamento de Física Aplicada, Universidad Politécnica de Madrid, Spain (2011), online article.
[25] L.H. Germer, “Electrical breakdown between close electrodes in Air,” J. Appl. Phys., 30(1), 1958 pp 46-51.
[26] M. Tichŷ, Langmuir Probe Diagnostics for Medium Pressure and Magnetised Low-Temperature Plasma, J. Phys. IV France, 7, C4-397-411 (1997).
[27] M. Tichý, Langmuir Probe Measurements of Spatial Plasma Profiles and Temporal Dependences in a DC-Energized Hollow-Cathode Plasma Jet System, J. Plasma Fusion Res. SERIES, 8, 1277-1282 (2009).

[28] M. Yusupov, Behavior of electrons in a dual-magnetron sputter deposition system: a Monte Carlo model, New J. of Physics, 13, 033018 (2011).
[29] M. Yusupov, Elucidating the asymmetric behavior of the discharge in a dual magnetron sputter deposition system, Appl. Phys. Lett., 98, 131502 (2011).
[30] M.A. Hassouba and N. Dawood, Study the Effect of Magnetic Field on the Electrical Characteristics of the Glow Discharge, Adv. in Appl. Sci. Res., 2(4), 123-131 (2011).
[31] M.B. Hendricks, Effects of ion-induced electron emission on magnetron plasma instabilities, J. Vac. Sci. Technol. A 12, 1408 (1994)
[32] M.H. Elghazaly, S. Solyman and A.M. Abdelbaky, Study of Some Basic Transport Coefficients in Noble-Gas Discharge Plasmas, Egypt. J. Solids, 30(1), 137 (2007).
[33] M.M. Mansour et al., "Effect of He and Ar Addition on N_2 Glow Discharge Characteristics and Plasma Diagnostics", Arab J. of Nuclear Sci. and Applications, 46(1), 116-125 (2013).
[34] O.A. Hammadi et al., "Employment of Magnetron to Enhance Langmuir Probe Characteristics of Argon Glow Discharge Plasma in Sputtering System", Iraqi J. Appl. Phys., 12(4) (2016) 19-28.
[35] O.A. Hammadi et al., "Magnetic Field Distribution of Closed-Field Unbalanced Dual Magnetrons Employed in Plasma Sputtering Systems", Iraqi J. Appl. Phys., 12(3) (2016) 35-42.
[36] O.A. Hammadi et al., "Operation Characteristics of a Closed-Field Unbalanced Dual-Magnetrons Plasma Sputtering System", Bulg. J. Phys., 41(1) (2014) 24-33.
[37] P. Kisliuk, "Electron emission at high fields due to positive ions," J. Appl. Phys., 30(1), (1958) 51-55.
[38] P.J. Kelly and R.D. Arnell, Magnetron sputtering: a review of recent developments and applications, Vacuum 56 (2000) 159-172.
[39] R. Arnell and P. Kelly, Recent advances in magnetron sputtering, Surf. Coat. Technol., 112, 170-176 (1999).
[40] R. Raju, Development and characterization of a secondary RF plasma-assisted closed-field dual magnetron sputtering system for optical coatings on large-area substrates, Plasma Sources Sci. Technol., 19, 025011 (2010).
[41] R.H. Stark and K.H. Schoenbach, "Direct current high-pressure glow discharge," J. Appl. Phys., 85(4) (1999) 2075-2080.
[42] R.L. Merlino, Understanding Langmuir probe current-voltage characteristics, Am. J. Phys., 75(12), 1078-1085 (2007).
[43] S.-H. Seo and H.-Y. Chang, Anomalous behaviors of plasma parameters in unbalanced direct-current magnetron discharge, Phys. Plasmas 11, 3595 (2004).
[44] T.E. Sheridan, M.J. Goeckner and J. Goree, Electron velocity distribution functions in a sputtering magnetron discharge for the ExB direction, J. Vac. Sci. Technol. A 16(4), 2173-2176 (1998).
[45] T.E. Sheridan, M.J. Goeckner and J. Goree, Model of energetic electron transport in magnetron discharges, J. Vac. Sci. Technol. A, 8(1), 30-37 (1990).
[46] Torres J.M. and Dhariwal R.S., "Electric field breakdown at micrometre separations," Nanotechnol., 10 (1999) 102-107
[47] U.H. Kwon, Multi-scale simulation of plasma generation and film deposition in a circular type DC magnetron sputtering system, Thin Solid Films, 475, 17– 23 (2005).
[48] V. Godyak, R.B. Piejak and B.M. Alexandrovich, "Electrical Characteristics of Parallel-Plate RF Discharges in Argon", IEEE Trans. on Plasma Sci., 19(4) (1991) 660-676.
[49] V.A. Godyak, R.B. Piejak and B.M. Alexandrovich, "Ion flux and ion power losses at the electrode sheaths in a symmetrical rf discharge," J. Appl. Phys. 69(6), March 1991, pp. 3455-3460
[50] V.A. Lisovskiy and V.D. Yegorenkov, "RF breakdown of low-pressure gas and a novel method for determination of electron-drift velocities in gases," J. Phys. D: Appl. Phys., 31 (1998) 3349-3357.
[51] van der Mullen. J. A. M., "Excitation equilibria in plasmas; a classification," Phys. Rep., (191) 109-220, 1990.
[52] Y.P. Raizer, "Gas Discharge Physics," Springer-Verlag, Berlin, 1991, Section 9.4.

IRAQI JOURNAL OF APPLIED PHYSICS
Vol. 18, No. 2, April-June 2022, pp. 23-26

Characteristics of Indium Nitride Thin Films Deposited on Silicon Substrates by Reactive Sputtering with Nitride Buffer Layers

Ali M. Hassan [1]
Ameer S. Hamad [2]
Kadhum A. Mhawsh [2]
Zaid M. Lazim [1]

[1] *Department of Medical Physics,*
Al-Hasseb University College,
Najaf, IRAQ
[2] *Department of Physics,*
College of Science,
Jabir bin Hayan University,
Basrah, IRAQ

In this work, nanostructured InN thin films were deposited on (100) silicon substrates using reactive sputtering technique. Moreover, two different nitride (GaN or AlN) films were deposited on the substrates before deposition of indium nitride to form a buffer layer. The structural characteristics of the prepared samples were studied by x-ray diffraction (XRD) and field-effect scanning electron microscopy (FE-SEM). As well, the photoluminescence (PL) spectra of the prepared samples were recorded. The XRD results indicated that all indium nitride films exhibited preferred growth orientation along the c-axis with different intermediate buffers. The photoluminescence characteristics indicated that the band gap of InN/GaN/Si is about 0.79 eV and of InN/AlN/Si is about 0.65 eV. These results indicate that the control of buffer layer is essential for engineering the growth of InN/Si structures.

Keywords: Indium nitride; Reactive sputtering; Thin films; Buffer layer
Received: 8 April 2022; Revised: 29 April 2022; Accepted: 6 May 2022

1. Introduction

Indium nitride is a potentially important material for optoelectronic and high speed electronic devices, due to its narrow band gap (<0.7 eV) [1] and superior properties [2], such as high electron mobility [3], small electron effective mass [4], and low carrier concentration [5,6]. The theoretical maximum mobility calculated for wurtzite indium nitride at 300 K is ~1.4x10^5 cm^2/V.s [7], while at 77 K the limits are beyond 3x10^5 cm^2/V.s. Indium nitride is expected to be used for fabrication of high performance high electronmobility transistors (HEMTS), light-emitting diodes (LEDs) and high efficiency solar cells [8]. The early studies reporting the indium nitride band gap to be ~2 eV were limited by material grown by RF sputtering [9]. Recent experiments performed on high-quality indium nitride films grown by molecular-beam epitaxy MBE have shown that the fundamental band gap of indium nitride is about 0.7 eV [10]. The discrepancy in band-gap could be attributed to the crystallinity, carrier concentration, defects, and impurities present in the indium nitride material [11, 12]. Although explanations including the incorporation of oxygen and the Burstein-Moss shift have been proposed, the actual roles of these effects have not been clarified. With the improvement of growth techniques in the past few years, as such as high-quality indium nitride epilayers grown by molecular beam epitaxy (MBE) [13], metal-organic molecular beam epitaxy (MOMBE) [14], sputtering [15], and metal organic chemical vapor deposition (MOCVD) [16] are now readily available. However, the growth of high quality indium nitride films is known to be difficult due to a lack of suitable substrates materials that are matched with indium nitride in terms of both lattice constant and thermal expansion coefficient [17]. Also, the main problems of producing indium nitride thin films are low dissociation temperature of indium nitride [18], and the high equilibrium vapor pressure of nitrogen and lattice mismatch between film and substrate. A variety of buffer layers on Si and sapphire substrates have been employed for the growth of indium nitride continuous film [19].

Compared with indium nitride and sapphire is far below the mismatch of 25.4%. As the result of large lattice mismatch, these structures contain a very high density of various defects. The effect of growth parameters of indium nitride films such as the substrate temperature, RF power, and indium/nitrogen flow ratio has been investigated to optimize sample quality [20]. Previous studies of indium nitride deposition on oxide layer show that indium nitride has the highly oriented in the *c*-axis direction [21]. The oxide buffer layer could be a suitable buffer layer for the growth of high-quality indium nitride films. Therefore, low lattice mismatch layer improved the indium nitride nucleation with a high quality [22]. Also, silicon is a very promising material for the growth of III-V materials. With its good thermal conductivity which is especially interesting for electronic applications [23] but also for low-cost high brightness light emitting diodes (LEDs) applications [24]. However, few studies report indicated that indium nitride thin films growth on (100) Si substrates using MOMBE.

In this work, we studied the effect of different buffer layers on the growth of indium nitride by reactive sputtering technique. We found that high quality indium nitride thin films can be deposited on silicon substrates using the buffer layer.

2. Experimental Work

Reactive sputtering was used to deposit indium nitride thin films on silicon substrates with and without deposition of buffer layers between indium nitride film and silicon substrate. Figure (1) shows schematic diagram of sputtering chamber used in this work. A highly-pure (0.999) indium target was mounted on the cathode while the silicon substrate was placed on the anode. The chamber was initially evacuated to a base pressure of 10^{-5} mbar by a diffusion pump. Argon gas was pumped into the chamber with average pressure of 0.8 mbar to be used as a working gas to generate the plasma. Ammonia was used as a reactive gas to provide atomic nitrogen required to form indium nitride compound. Before loading substrate into the chamber, the Si(100) substrates were cleaned in an ultrasonic bath with acetone and ethanol, and the Si(100) substrates were also etched in a 5% HF solution for 3min to remove the oxide on the surface.

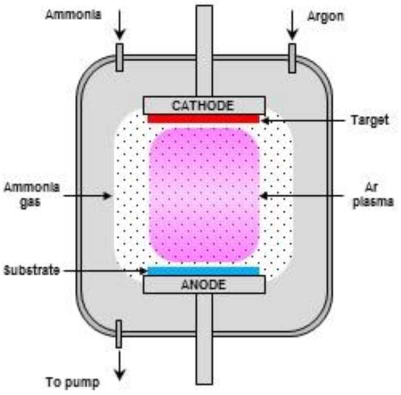

Fig. (1) Schematic diagram of sputtering chamber used in this work

Before deposition of aluminum nitride film as a buffer layer, the temperature of silicon substrate was increased up to 800°C to support the formation of aluminum nitride layer and induce its adhesion to the substrate. The substrate temperature was kept at 200°C during the deposition of gallium nitride layer. During the deposition, the substrate temperature was monitored by a thermocouple.

The x-ray diffraction (XRD) patterns were recorded using a Bruker x-ray diffractometer with a CuKα radiation source. The surface morphologies and cross-section of prepared samples were obtained by a Fisher-Scientific Phenom XL G field-emission scanning electron microscopy (FE-SEM). The photoluminescence (PL) measurements were performed using a diode laser operating at a wavelength of 976nm as the excitation source.

3. Results and Discussion

Figure (2) shows the XRD patterns of the InN films, InN/AlN and InN/GaN structures deposited on (100) silicon substrates. The observed diffraction peak exhibited dominant InN (0002) peak at 31.3° for all samples, revealing that the InN films mainly consisted of the hexagonal InN phase.

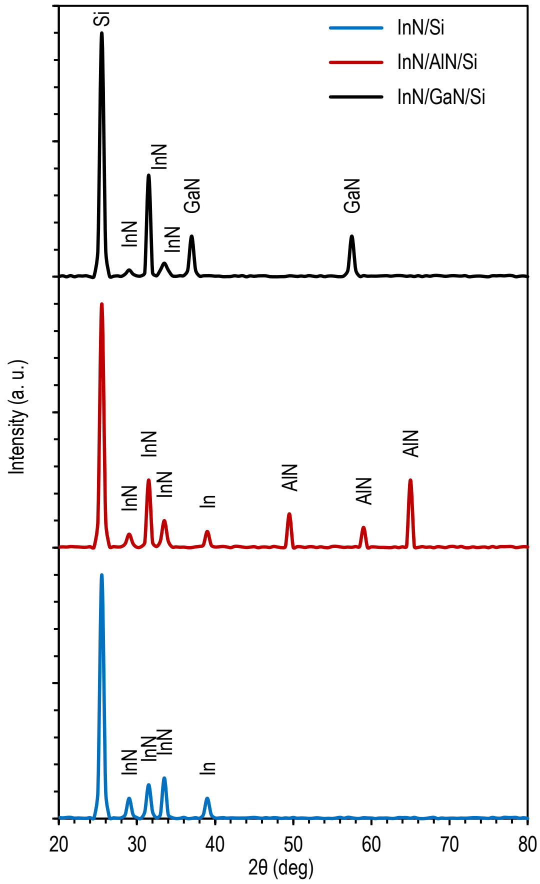

Fig. (2) XRD patterns of (a) InN films, (b) InN/AlN structure, and (c) InN/GaN structure deposited on (100) silicon substrates

Diffraction peaks corresponding to the (0002) and (0004) from InN film, and the (400) diffraction peak from (100) Si are observed for InN/Si sample. Compared with direct deposition on Si(100) substrate, the InN/GaN exhibited highly *c*-axis preferred orientation indicating that it have relative narrow peak with good crystalline quality. In addition, InN grown on AlN layer and (100) Si substrate exhibited polycrystalline structure and random growth. Also, a smaller peak corresponding to the indium metal detected in the XRD pattern for InN/AlN and InN/Si samples, which is probably due to the slightly In-rich conditions. Also, three prominent XRD peaks, corresponding to InN (100), (0002), (101), and In(101) were observed for InN film grown directly on the Si substrate, while there is no indium oxide peak in the XRD spectra. According to these results, the GaN buffer layer can provide InN nucleation and improvement quality due to smaller lattice mismatch (~8.9%). From the observed (0002) diffraction the lattice parameter *c* can be obtained. InN/GaN structure shows the large than the value of the bulk crystal [25,26] attributed to the residual strain in the InN film.

Figure (3) shows the plane-view and cross-sectional FE-SEM images of InN films deposited on various buffer layers. Cross-section image of InN/GaN structure indicated that thickness of GaN layer is about 240nm. The image reveals that the InN/GaN structure exhibits a pronounced columnar-structure. Also, surface morphology of InN film shows the needle-like nanocrystals. In addition, an InN/AlN structure reveals the granular structure of surface morphology. Also, surface roughness is larger than InN deposited on GaN layer due to high density grain boundaries and island growth.

The InN film directly deposited on silicon substrate exhibits surface morphology of non-continuous and rough features. The result is due to a stress induced 3D-growth mechanism caused by a lattice strain and/or higher desorption rate. Also, the formation of metallic indium on the surface was observed which corresponding to XRD result.

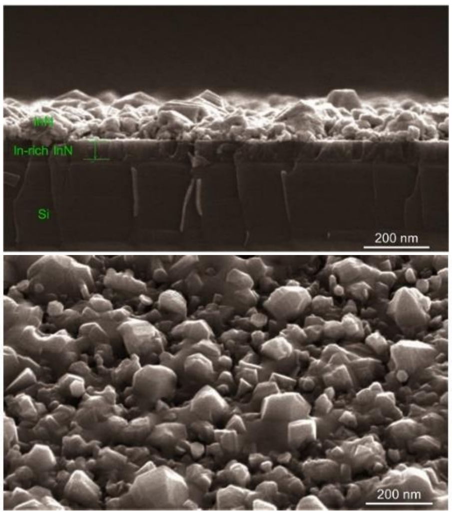

(a)

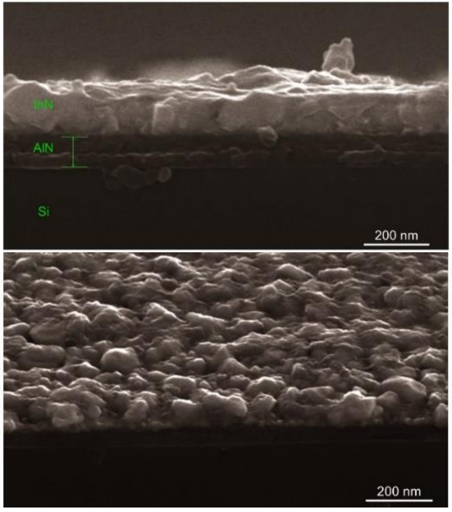

(b)

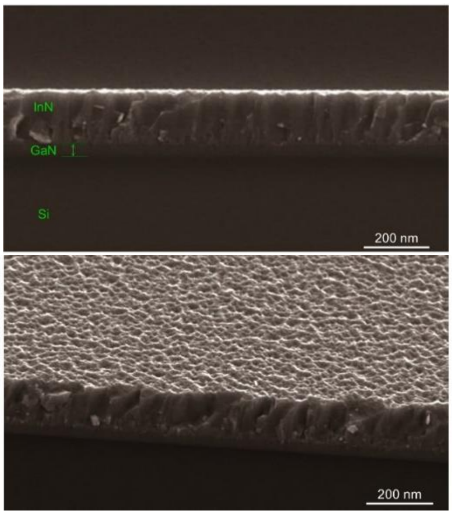

(c)

Fig. (3) SEM cross-sectional and surface morphologies images of (a) InN films, (b) InN/AlN structure, and (c) InN/GaN structure deposited on (100) silicon substrates

Figure (4) shows the PL spectra recorded at room temperature from an InN film deposited on GaN or AlN layer. The PL result indicated fundamental band gap of about 0.79 eV for InN/GaN structure and about 0.65 eV for InN/AlN structure. In contrast to previous studies [27], InN grown on oxide layer exhibited large band gap due to high carrier density and oxygen incorporation [28]. Also, the origin of the higher measured band gaps in these films can be attributed to the presence of In_2O_3 (E_g=3.75 eV) [29] inclusions and, perhaps, to a blue-shift of the absorption edge from quantum-size effects caused by the needle-like [30,31]. In addition, the intrinsic defects such as N vacancies and/or dislocations could be important additional sources for free electrons in these samples.

The Hall measurements of the prepared InN/GaN structure exhibited a high carrier concentration of 2.6×10^{20} cm^{-3} and electron mobility of 78 $cm^2/V.s$. Therefore, we infer that fewer defects and the low background carrier concentration were cause of influence high quality InN.

4. Conclusion

In summary, the high quality InN thin films deposited on (100) silicon substrates with the GaN buffer layer is critical to achieve nucleation and duplicate orientation. The InN films are highly oriented in the *c*-axis direction. The GaN buffer layer improved the crystal quality effectively which was smaller surface roughness. The PL results reveal that band gap of InN/gaN structure was about 0.79 eV. Also, the high background-carrier concentration may be caused by a structural defect and/or oxygen incorporation.

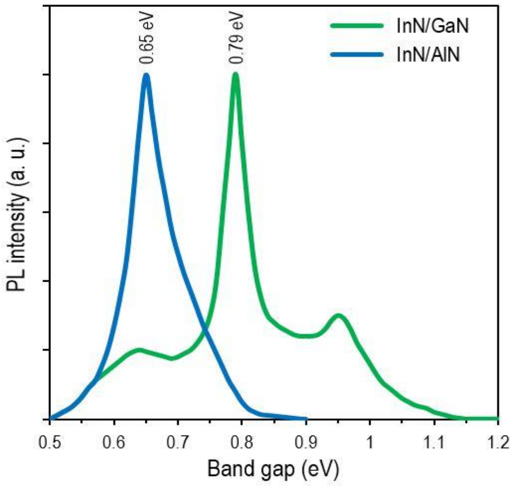

Fig. (4) PL spectra of InN films deposited on (100) Si substrates with different buffer layers at room temperature

References

[1] A.K. Murali, A.D. Barve and S.H. Risbud, “A kinetic study of indium nitride formation from indium oxide powders”, Mater. Sci. Eng. B, 96(2) (2002) 111-114.
[2] B.R Nag, “Electron mobility in indium nitride”, J. Cryst. Growth, 269(1) (2004) 35-40.
[3] C.G. Rodrigues, “Nonlinear electronic transport behavior in Indium Nitride”, Mater. Chem. Phys., 137(1) (2012) 317-322.
[4] Das and R.K. Yadav, “The influence of transition metal (Mn, Fe, Co, Cu)doping on the electronic and vibrational properties of indium nitride nanocage: A DFT study”, Comp. Theor. Chem., 1205 (2021) 113447.
[5] G.B. Damas et al., “Understanding indium nitride thin film growth under ALD conditions by atomic scale modelling”, Appl. Surf. Sci., 592 (2022) 153290.
[6] H. Timmers et al., “Compositional and structural characterization of indium nitride using swift ions”, J. Cryst. Growth, 288(2) (2006) 236-240.
[7] H. Timmers, S.K. Shrestha and A.P. Byrne, “The potential of ion beam techniques for the development of indium nitride”, J. Cryst. Growth, 269(1) (2004) 50-58.
[8] H.S. Lee et al., “Sol–gel spin coating growth of magnesium-doped indium nitride thin films”, Vacuum, 155 (2018) 16-22.
[9] J. Jalilian et al., “Tuning of the electronic and optical properties of single-layer indium nitride by strain and stress”, Phys. E: Low-dimensional Systems and Nanostr., 83 (2016) 372-377.
[10] L. Wang et al., “Chemical synthesis of hexagonal InN nanocrystallines at low temperature”, J. Cryst. Grow, 471 (2017) 62-65.
[11] M. Ohkubo et al., “Optical properties of amorphous indium nitride films and their electrochromic and photodarkening effects”, Appl. Surf. Sci., 113-114 (1997) 476-479.
[12] M.A. Qaeed et al., “Optical and structural properties of indium nitride nanoparticles synthesized by chemical method at low temperature”, Solar Energy, 97 (2013) 614-619.
[13] M.V.S. da Silva et al., “Structural, optical and electrical properties of indium nitride polycrystalline films”, Thin Solid Films, 520(15) (2012) 4848-4852.
[14] P. Becker and R. Niewa, “Progress in ammonothermal crystal growth of indium nitride”, J. Cryst. Growth, 581 (2022) 126480.
[15] P.P.-T. Chen et al., “Effects of crystallinity and chemical variation on apparent band-gap shift in polycrystalline indium nitride”, Thin Solid Films, 519(6) (2011) 1831-1836.
[16] Q. Guo et al., “Effect of the substrate pretreatment on the epitaxial growth of InN”, Appl. Surf. Sci., 169-170 (2001) 345-348.
[17] O.A. Hammadi, “Effects of Extraction Parameters on Particle Size of Titanium Dioxide Nanopowders Prepared by Physical Vapor Deposition Technique”, Plasmonics, 15 (2020) 1747-1754.
[18] R. Chandiramouli and S. Sriram, “Investigation on band structure and electronic transport properties of indium nitride nanoribbon – A first-principles study”, Superlat. Microstr., 65 (2014) 22-34.
[19] R.-S. Chen et al., “Electronic transport properties in aluminum indium nitride nanorods grown by magnetron sputter epitaxy”, Appl. Surf. Sci., 285(Part B) (2013) 625-628.
[20] R.T Shamrell and C. Parman, “Optical properties of reactively sputtered indium nitride thin films”, Opt. Mater., 13(3) (1999) 289-292.
[21] S. Ben Khalifa et al., “Growth study of thin indium nitride layers on InP (100) by Auger electron spectroscopy and photoluminescence”, J. Cryst. Growth, 311(9) (2009) 2608-2614.
[22] S. Kosaraju et al., “The role of argon in plasma-assisted deposition of indium nitride”, J. Cryst. Growth, 286(2) (2006) 400-406.
[23] S. Wakasugi et al., “Structural studies in the epitaxial-growth of InN crystals with flower-like structure on a sapphire (112¯0) substrate”, Solid State Sci., 9(11) (2007) 1000-1005.
[24] S.J. Patil et al., “Characterization of indium nitride films deposited by activated reactive evaporation process”, Thin Solid Films, 444(1-2) (2003) 52-57.
[25] S.J. Patil et al., “Deposition of indium nitride films by activated reactive evaporation process – a feasibility study”, Appl. Surf. Sci., 245(1-4) (2005) 73-78.
[26] S.K. Shrestha and H. Timmers, “The optimum heavy ion beam for the compositional analysis of indium nitride films”, Nucl. Instrum. Meth. in Phys. Res. B: Beam Interactions with Materials and Atoms, 249(1-2) (2006) 257-260.
[27] W.-N. Hsu and T.-S. Shih, “Effect of the nanoscratch resistance of indium nitride thin films in the etching duration”, Appl. Surf. Sci., 261 (2012) 610-615.
[28] W.Z. Shen et al., “Critical point transitions of wurtzite indium nitride”, Solid State Commun., 137(1-2) (2006) 49-52.
[29] Z.H Lan et al., “Growth mechanism, structure and IR photoluminescence studies of indium nitride nanorods”, J. Cryst. Growth, 269(1) (2004) 87-94.
[30] Z.Y. Lee et al., “Influences of elevated thermal decomposition of ammonia gas on indium nitride grown by sol–gel spin coating method”, Mater. Res. Bull., 96(3) (2017) 258-261.
[31] Z.Y. Lee, S.S. Ng and F.K. Yam, “Growth mechanism of indium nitride via sol–gel spin coating method and nitridation process”, Surf. Coat. Technol., 310 (2017) 38-42.

IRAQI JOURNAL OF APPLIED PHYSICS
Vol. 18, No. 2, April-June 2022, pp. 27-32

Fluorescence Characteristics of Highly-Pure Nanoparticles Embedded in Dye Complexes for Random Laser Design

Atheer A. Mahmood [1]
Haitham M. Mikhlif [2]
Oday A. Hammadi [3]

*[1] Department of Chemistry,
College of Education,
Al-Iraqia University,
Baghdad, IRAQ*
*[2] Department of Physics,
College of Science,
Mustansiriyah University,
Baghdad, IRAQ*
*[3] Department of Physics,
College of Education,
Al-Iraqia University,
Baghdad, IRAQ*

In this work, highly-pure titanium dioxide nanoparticles produced by dc magnetron sputtering technique were embedded in coordination complex solutions such as Baq_2 or Znq_2 to form random gain media. The structural characteristics of the TiO_2 nanoparticles were determined to confirm their high structural purity. The spectroscopic characteristics, mainly photoluminescence and fluorescence, of the complex solutions containing the nanoparticles were determined and studied. These media were compared to two of the most common laser dyes (Rhodamine B and Rhodamine 6G) to determine the feasibility of using them to produce random laser.

Keywords: Metal complex; Fluorescence; Photoluminescence; Nanoparticles; Random laser
Received: 24 March 2022; **Revised:** 13 May 2022; **Accepted:** 20 May 2022

1. Introduction

Recently, fluorescence has become one of the most important techniques in characterization and diagnosis in applied and experimental sciences due to its sensitivity, ease of use, and versatility. Fluorescence is the emission of light from any substance and occurs from electronically excited singlet states, while phosphorescence is the emission of light from triplet excited states [1].

The 8-hydroxyquinoline (8-HQ), commonly known as oxine, is the most popular among the hydroxyquinolines due to its excellence in complex formation with metal ions and with a wide spectrum [2,3]. Fluorescence features of hydroxyquinoline with metals have been done by Feigl and Heisig [4]. The metal chelates of 8-hydroquinoline arouse a wide interest because of structure and fluorescence characteristics [5,6]. The role of nano-sized gold on fluorescence properties of Rh6G has been analyzed by using steady state and time resolved fluorescence methods [7]. The bis(8-hydroxyquinoline) zinc has been provided to be used for high-efficiency working voltage OLEDs [8-10].

Nanoparticles of metal oxide have attracted great attention in recent years because of their benefits in long-term programs of environmental remediation and digital devices. They have been broadly utilized in solar cells, piezoelectric nanogenerators, optoelectronic devices, UV detectors, photocatalysis, etc. due to their extended band gap, insolubility, and small sizes [11-15]. Titanium dioxide has been used as a photocatalytic due to its numerous advantages which consist of high chemical and optical stabilities, low charge and toxicity [16,17].

The aim of this work is to synthesize some coordination dye complexes and compare their fluorescence and photoluminescence characteristics to those of some common laser dyes to fabricate random laser.

2. Experimental Part

The complexes were synthesized by adding 2.9 g of 8-hydroxyquinoline which was dissolved in a mixture of (potassium hydroxide 1.12 g with distilled water), then it was stirred well. A 1.36 g sample of every salt ($BaCl_2.2H_2O$ and $ZnCl_2$) were dissolved in distilled water and stirred well. Theses aqueous solutions were mixed with solution in the first step and the remaining mixture with stirring for 20 min. Each complex was prepared by 1:2 ratios. Finally, product was dried at oven for six hours after washing in distilled water.

In order to form the random gain media, highly-pure titanium dioxide nanoparticles with minimum size of particles about 25 nm were mixed with the complex solution. Then spectra of absorption and photoluminescence were measured and compared before and after mixing nanoparticles with the complex. The preparation conditions were determined after conducting many experiments to know through which the minimum amount of nanoparticles (500 μg) that can be added to 5×10^{-3} L complex solution of 10^{-5} M concentration.

The ligands and synthesized complexes were characterized by measuring absorption spectra which recorded using UV-Visible double-beam SPEKOL2000 instrument in a spectral range of 190-1100 nm. These measurements were carried out on the samples in ethanol. In order to study the effects of size and distribution of nanoparticles on the characteristics of the prepared samples, field-emission scanning electron microscopy (FE-SEM) was employed. The photoluminescence (PL) properties of complexes were measured by Hitachi F-

7000f fluorescence spectrometer with 150 W monochromatic xenon lamps as the excitation source.

In this work the dc reactive magnetron sputtering system used for synthesis of nanostructures. The operation parameters were optimized, more details can be found elsewhere [18-22]. The nanopowder was extracted from the titanium dioxide thin film samples prepared in this work by ultrasonic waves-assisted conjunctional freezing technique [23,24].

The film thickness can be controlled by determining the deposition time, However, the optimum samples were prepared using gas mixing ratio (Ar:O_2) of 1:1, inter-electrode distance of 4 cm, and deposition time of two hours. The structural and spectroscopic characteristics of these samples were determined by x-ray diffraction (XRD), field emission scanning electron microscopy (FE-SEM), energy-dispersive x-ray spectroscopy (EDX), UV-visible and Fourier-transform infrared (FTIR) spectroscopy, fluorescence and photoluminescence spectroscopy.

The absorbance spectrum is created by exciting electrons at varying wavelengths while monitoring the emission at a fixed wavelength. The results from an absorbance spectrum is valuable in determining the fixed excitation wavelength for the emission spectrum. Photoluminescence (PL) spectroscopy is a form of light emission spectroscopy in which the light emission originates from a process called photo-excitation. As the light is directed onto a sample, the electrons within the material move into excited states. When the electrons come down from the excited states to their equilibrium states, the energy can be released in the form of light.

3. Results and Discussion

Figure (1) explain the XRD pattern of TiO_2 thin film sample prepared in this work. It is clear that the sample exhibits high structural purity as no peaks belonging to other materials than TiO_2 are observed. In TiO_2 sample, both phases (rutile; R and anatase; A) are recognized [25], however, the anatase phase is apparently dominant as the crystal planes belonging to anatase TiO_2 are more than those belonging to rutile TiO_2.

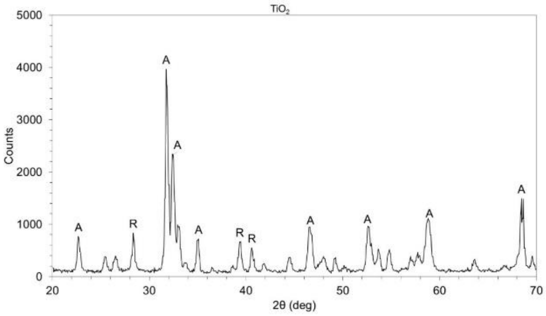

Fig. (1) XRD pattern of TiO_2 nanopowder extracted from thin film samples

Further confirmation of the structural purity of the prepared samples can be presented by the FTIR results, see Fig. (2). The main peaks belonging to the vibration of Ti-O and O-Ti-O are observed with additional peaks belonging to the O-H group resulting from the exposure to the environment [26-29] which enhance its performances involving photogenerated current, photocatalysis and energy storage [30]. Therefore, the prepared sample can be described as highly-pure structure. The presence of titanium dioxide nanoparticles can be observed by comparing the FTIR spectrum before and after adding nanoparticles to the complexes as can be seen in the figures (3a-d).

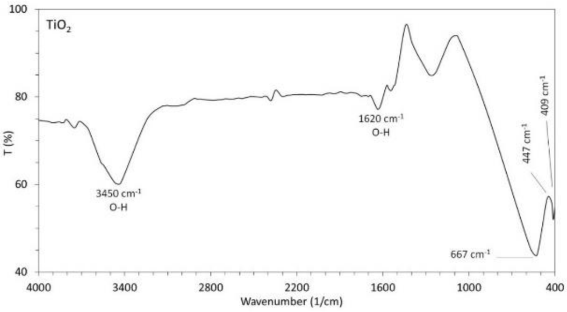

Fig. (2) FTIR spectrum of TiO_2 nanopowder extracted from thin film samples

Surface profile and particle size for the prepared thin films were determined by field emission scanning electron microscopy (FE-SEM). Fig. (4) states FE-SEM image of TiO_2 nanopowder of thin film sample prepared using Ar:O_2 mixture of 50:50 mixing ratio and inter-electrode distance of 4 cm after deposition time of one hour. The first feature can be seen in these images is the homogeneity of particles distribution which is one of the most important advantages of dc magnetron sputtering technique used for synthesis of nanostructures. Another important feature is the absence of aggregation over the scanned sample. In the mixed-phase TiO_2 sample, the 13 crystal planes can form intertwined facets and hence the inter-space between nanoparticles may be minimized and the nanosurface appears much more flatn than the single-phase sample [31]. A minimum particle size of about 40 nm can be noticed with no large aggregation. The energy-dispersive x-ray (EDX) spectrum for titanium dioxide nanopowder extracted from this thin film sample is shown in Fig. (5). The elemental compositions in the final samples is presented in the table below the figure. With the existence of Ti and O in the final sample, the percentage weights of Ti and O was found to be 46.77 and 50.79, respectively. This result confirmed the stoichiometry of the TiO_2 molecules which completely agrees with the chemical bonding configuration of such compound. In this sample, no impurities were detected as supported by the atomic integration of Ti and O elements. This feature is highly preferred for studies concerned to the concepts of physical and chemical characteristics and processes [22].

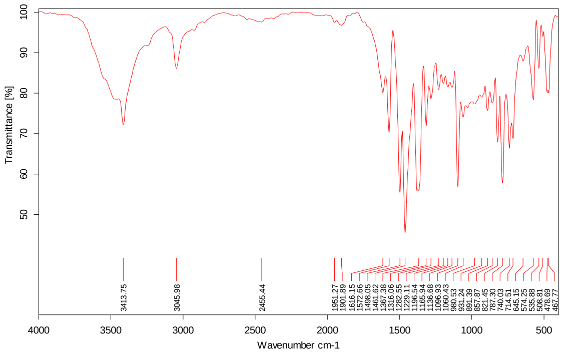

(a) Baq_2

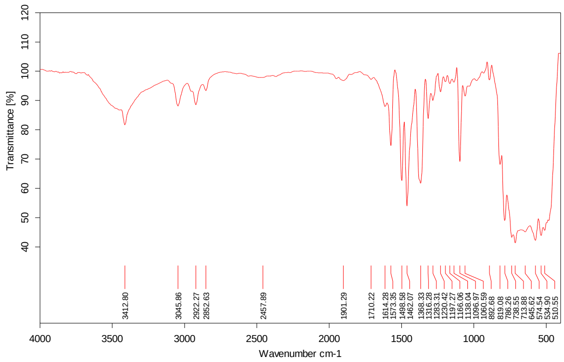

(b) Baq_2 after adding TiO_2 NPs

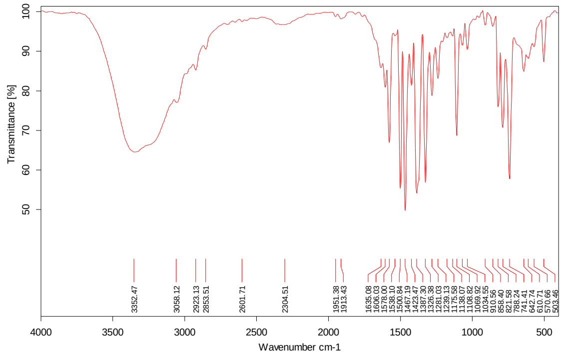

(c) Znq_2

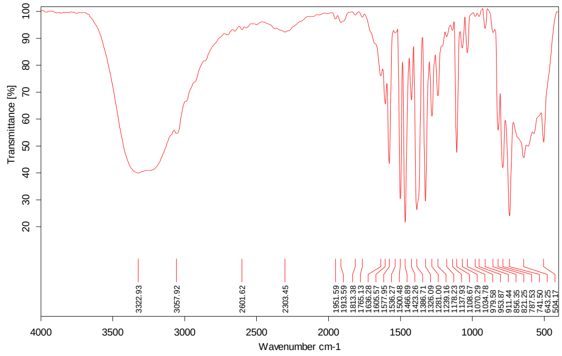

(d) Znq_2 after adding TiO_2 NPs

Fig. (3) FTIR spectra of prepared complexes before and after adding TiO_2 NPs

Figure (6) indicates the absorption spectra of the Baq_2 and Znq_2 complexes in ethanol solvent before and after adding nanoparticles. It is apparent that the absorption peak for Baq_2 complex at 326 nm, changed after adding the nanoparticles. However, the absorbance of all complexes increases in the ultraviolet region (<300nm) for Baq_2 complex and another increase for Znq_2 recorded in spectral range 500-800 nm as well after adding the nanoparticles.

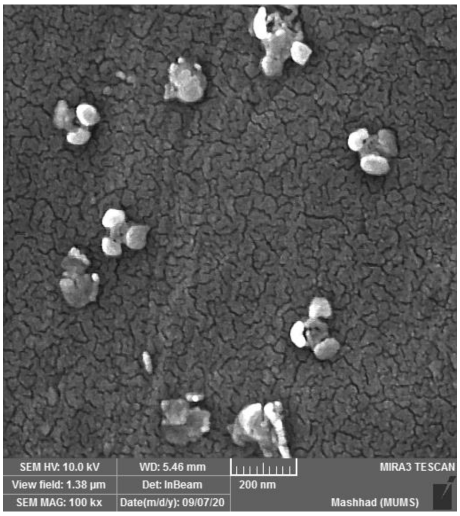

Fig. (4) SEM image of TiO_2 nanopowder extracted from thin film samples

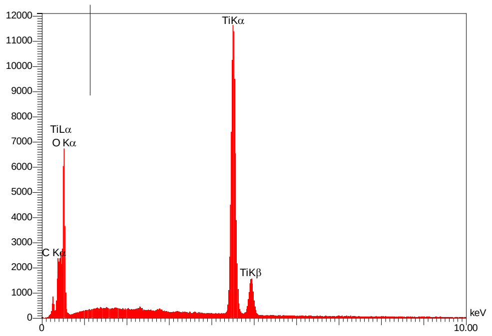

Element	Line	Intensity	W%	A%
C	Ka	80.0	2.44	4.67
O	Ka	670.5	50.79	72.91
Ti	Ka	2361.4	46.77	22.42
			100.00	100.00

Fig. (5) EDX spectrum of TiO_2 nanopowder extracted from thin film samples

Both cases – before and after adding the nanoparticles – photoluminescence spectra of the coordination complexes were recorded and compared as shown in Fig. (7). All complexes have distinct peaks; the primary in the blue region from 450 to 470 nm and the second one in the region from 510 to 515 nm. In the Baq_2 complex, the width of the primary peak changed into better than that of the second one, in comparison to the Znq_2 wherein the width of the second peak changed into better than that of the primary one.

For the Baq_2 complex, it is clear that adding the nanoparticles leads to a slight increase (~2.4%) in the PL intensity at peak of 457nm of the Baq_2 alone and reaches to 23% at 661 nm as shown in Fig. (7a). This increase is attributed to the role of nanoparticles added to the complex solution as they provide more excited states for electrons to reach as a result of photoexcitation. Thus, The photoluminescence of medium (Baq_2+NPs) is higher than Baq_2. Similar behavior was observed in Znq2 complex solution containing TiO_2 nanoparticles as the photoluminescence intensity at the peak wavelength of 471nm higher than Znq_2 as in Fig. (7b). However, the percentage increase in photoluminescence intensity is more than 27% due to adding nanoparticles to the complex solution. This difference in percentage increase may be ascribed to the matching between Znq_2 molecules and TiO_2 nanoparticles, which seems better than that between Baq_2 molecules and TiO_2 nanoparticles.

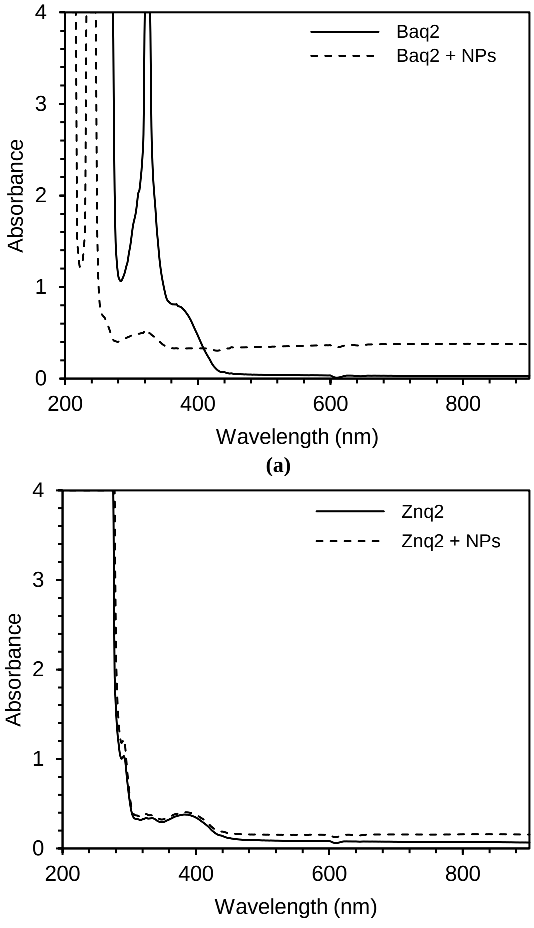

(a)

(b)

Fig. (6) Absorption spectra of (a) Baq_2 complex and (b) Znq_2 complex, before and after adding TiO_2 NPs

Since the aim of this work is to synthesize dye complexes for spectroscopic applications, mainly random gain media, then the fluorescence spectra of both complexes (Baq_2 and Znq_2) were compared to some standard laser dyes whose emission ranges are close to those of the complexes. Therefore, the fluorescence spectrum of the Baq_2 was compared to that of Rhodamine B dye while the fluorescence spectrum of the Znq_2 complex was compared to that of Rhodamine 6G dyes, as shown in Fig. (8).

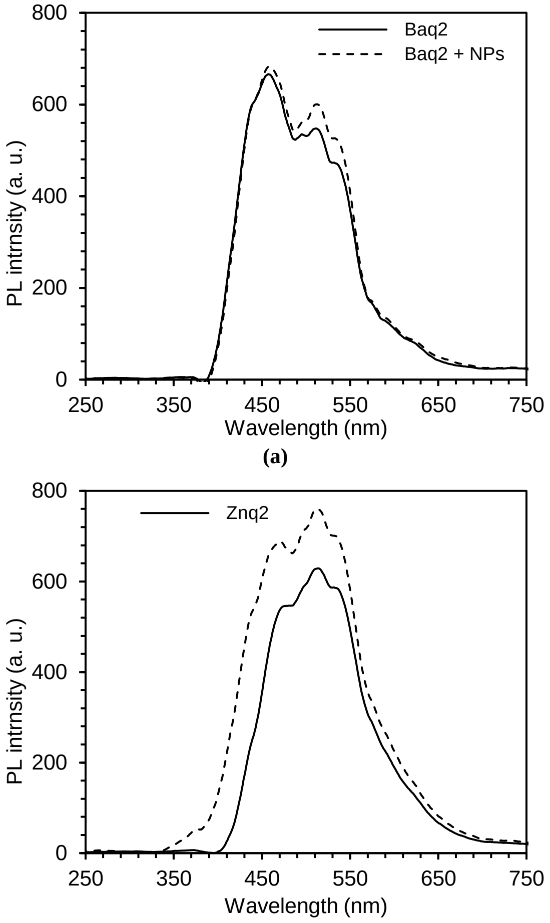

(a)

(b)

Fig. (7) Photoluminescence spectra of (a) Baq_2 complex and (b) Znq_2 complex, before and after adding TiO_2 NPs

As can be seen in Fig. (8a), the maximum of fluorescence intensity of the Baq_2 complex is about 43% of Rhodamine B at the same peak wavelength (610 nm). Similarly, the maximum intensity of fluorescence spectrum of the Znq_2 complex is about 65% that of Rhodamine 6G at the same peak wavelength (570 nm) as in Fig. (8b). Also, the spectral width for both complexes (Baq_2 and Znq_2) is reasonably larger than that of laser dyes (RB and R6G, respectively). This width can be narrowed using optical components such as etalons when the complex is employed as a laser active medium.

In order to fabricate random gain media from the synthesized complexes, highly pure titanium dioxide (TiO_2) nanoparticles were added to each complex, fluorescence spectra were recorded and compared to their spectra before adding these nanoparticles, as shown in Fig. (9).

It can be clearly seen from Fig. (9a) the effect of nanoparticles on the fluorescence spectrum of the Baq_2 complex. This effect is attributed to the increase in absorption because the nanoparticles act as trapping centers to the incident photons those would suffer from extremely higher path lengths throughout the complex sample. This increases the probability of absorbance and hence improving emission intensity.

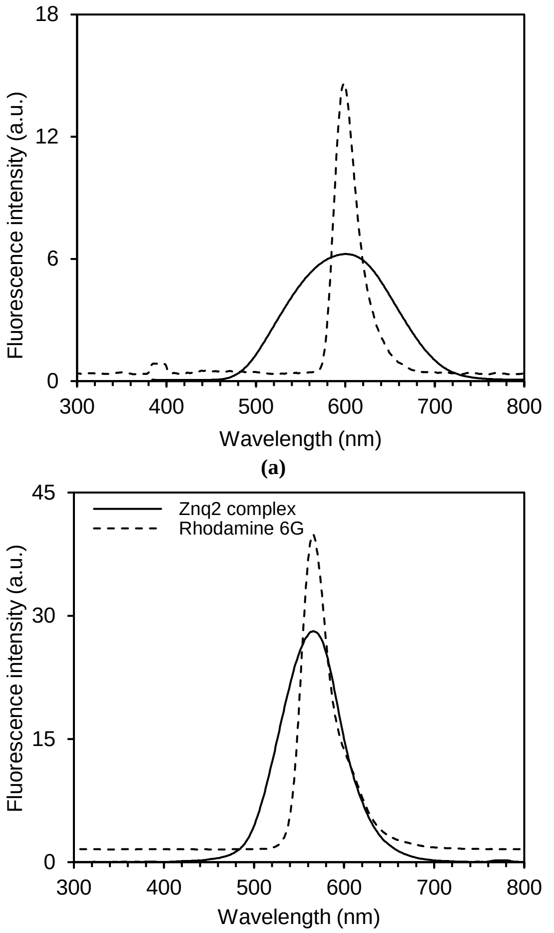

(a)

(b)

Fig. (8) Fluorescence spectra of (a) Baq_2 complex and (b) Znq_2 complex, compared to those of Rhodamine B and Rhodamine 6G, respectively

On the other hand, the effect of adding nanoparticles to the Znq_2 can be neglected as no variation can be observed in the fluorescence spectrum shown in Fig. (9b). This may be attributed to the high absorption of Znq_2 molecules to the incident photons before trapped by the nanoparticles added to the complex sample. Another possible reason is the formation of Zn nanoparticles within the complex, so they play the same role of TiO_2 nanoparticles (as in Baq_2 sample). Therefore, these nanoparticles would not contribute to the emission.

Apparently, the Baq_2 complex solution containing highly pure TiO_2 nanoparticles is better to fabricate random gain media than Znq_2, while Znq_2 complex solution is better to replace the Rhodamine 6G in conventional dye laser design.

4. Conclusion

The spectroscopic characteristics of coordination complexes such as Baq_2 and Znq_2 can be enhanced by adding highly-pure nanoparticles. Such nanoparticles can be efficiently produced by dc magnetron sputtering technique. The effects of adding these nanoparticles to the complex solutions were apparently observed by the enhancement of photoluminescence and fluorescence characteristics. As a conclusion, the media fabricated from highly-pure TiO_2 nanoparticles embedded in a coordination complex, such as Baq_2 or Znq_2, can be used to design and fabricate random gain media.

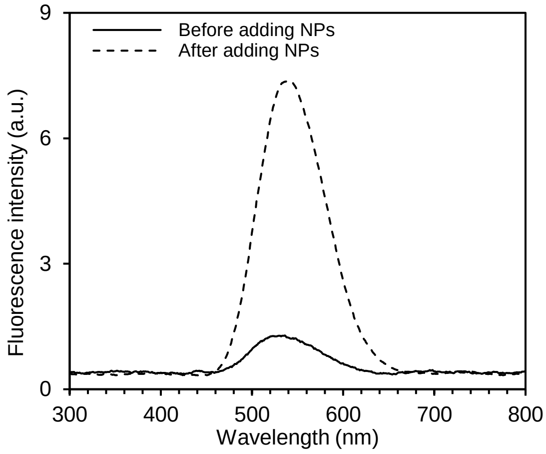

(a) Baq_2

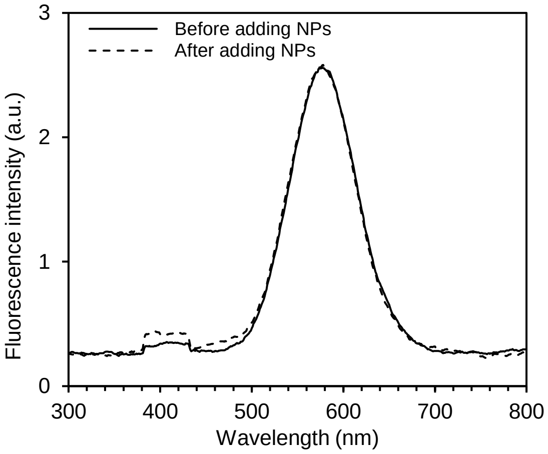

(b) Znq_2

Fig. (9) Fluorescence spectra of (a) Baq_2 complex and (b) Znq_2 complex, before and after adding TiO_2 NPs

References

[1] F. Xie, M. Baker and E.M. Goldys, “Enhanced Fluorescence Detection on Homogeneous Gold Colloid Self-Assembled Monolayer Substrates”, Chem. Mater., 20(5) (2008) 1788-1797.

[2] O. Popovych and L.B. Rogers, “Fluorescence in the 8-quinolinol family and the n-π transition”, Spectrochim. Acta, 15 (1959) 584-592.

[3] M.P. Bratzel et al., “Investigation of excited singlet state properties of 8-hydroxyquinoline and its derivatives by fluorescence spectrometry”, Anal. Chem., 44(7) (1972) 1240-1245.

[4] F. Fiegl and G.B. Heisig, “Analytic aspects of the chemical behavior of 8-hydroxyquinoline”, Anal. Chimica Acta, 3 (1949) 561-566.

[5] L.G. Zhang et al., “Effect of Metal Cation on Absorption and Fluorescence Spectra of Metal

Complexes of 8-Hydroxyquinoline", Scpectro. Lett., 29(6) (1996) 995-1001.

[6] M.D. Prat et al., "Fluorescence of Metal Complexes of 8-Hydroxyquinoline Derivatives in Aqueous Micellar Media", J. Fluorescence, 4(4) (1994) 279-281.

[7] B. Karthikeyan, "Fluorescence quenching of rhodamine-6G in Au nanocomposite polymers", J. Appl. Phys., 108(8) (2010) 084311.

[8] C.H. Chen and J.M. Shi, "Metal chelates as emitting materials for organic electroluminescence", Coordin. Chem. Rev., 171 (1998) 161-174.

[9] Y. Hamada et al., "Organic Electroluminescent Devices with 8-Hydroxyquinoline Derivative-Metal Complexes as an Emitter", Jpn. J. Appl. Phys., 32(4A) (1993) L514-L515.

[10] L.S. Sapochak, F.E. Benincasa and R.S. Schofield, "Electroluminescent Zinc(II) Bis(8-hydroxyquinoline): Structural Effects on Electronic States and Device Performance", J. Am. Chem. Soc., 124(21) (2002) 6119-6125.

[11] M.M. Rahman et al., "A comparative study on the photocatalytic degradation of industrial dyes using modified commercial and synthesized TiO_2 photocatalysts", J. Chem. Eng., 27(2) (2014) 65-71.

[12] A.O. Ibhadon, and P. Fitzpatrick, "Heterogeneous photocatalysis: recent advances and applications", Catalysts, 3(1) (2013) 189-218.

[13] A. Gnanaprakasam, V.M. Sivakumar and M. Thirumarimurugan, "Influencing parameters in the photocatalytic degradation of organic effluent via Nano metal oxide catalyst: a review", Ind. J. Mater. Sci., (2015) Article ID 601827.

[14] N.M. Julkapli, S. Bagheri and S.B.A. Hamid, "Recent advances in heterogeneous photocatalytic decolonization of synthetic dyes", Sci. World J., (2014) Article ID 692307.

[15] A.J. Attia, S.H. Kadhim and F.H. Hussein, "Photocatalytic degradation of textile dyeing wastewater using titanium dioxide and zinc oxide", J. Chem., 5 (2008) Article ID 876498.

[16] Q. Wang et al., "CuS, NiS as co-catalyst for enhanced photocatalytic hydrogen evolution over TiO_2", Int. J. Hydrog. Energy, 39(25) (2014) 13421-13428.

[17] J. Yin et al., "Fabrication of heterojunction $SnO_2/BiVO_4$ composites having enhanced visible light photocatalystic activity", Mater. Sci. Semicond. Process. 34 (2015) 198-204.

[18] O.A. Hammadi et al., "Operation Characteristics of a Closed-Field Unbalanced Dual-Magnetrons Plasma Sputtering System", Bulg. J. Phys., 41(1) (2014) 24-33.

[19] O.A. Hammadi et al., "Employment of Magnetron to Enhance Langmuir Probe Characteristics of Argon Glow Discharge Plasma in Sputtering System", Iraqi J. Appl. Phys., 12(4) (2016) 19-28.

[20] E.A. Al-Oubidy and F.J. Al-Maliki, "Effect of Gas Mixing Ratio on Energy Band Gap of Mixed-Phase Titanium Dioxide Nanostructures Prepared by Reactive Magnetron Sputtering Technique", Iraqi J. Appl. Phys., 14(4) (2018) 19-23.

[21] F.J. Al-Maliki, O.A. Hammadi and E.A. Al-Oubidy, "Optimization of Rutile/Anatase Ratio in Titanium Dioxide Nanostructures prepared by DC Magnetron Sputtering Technique", Iraqi J. Sci., 60 (Special Issue) (2019) 91-98.

[22] F.J. Al-Maliki and E.A. Al-Oubidy, "Effect of gas mixing ratio on structural characteristics of titanium dioxide nanostructures synthesized by DC reactive magnetron sputtering", Physica B: Cond. Matter, 555 (2019) 18-20.

[23] O.A. Hammadi, "Production of Nanopowders from Physical Vapor Deposited Films on Nonmetallic Substrates by Conjunctional Freezing-Assisted Ultrasonic Extraction Method", Proc. IMechE, Part N, J. Nanomater. Nanoeng. Nanosys., 232(4) (2018) 135-140.

[24] O.A. Hammadi, "Effects of Extraction Parameters on Particle Size of Titanium Dioxide Nanopowders Prepared by Physical Vapour Deposition Technique", Plasmonics, 15 (2020).

[25] M. Ladd and R. Palmer, "Structure Determination by X-Ray Crystallography", 5th ed., Springer (NY), 2013, p. 568.

[26] N.N. Greenwood and E.J.F. Ross, "Index of Vibrational Spectra of Inorganic and Organometallic Compounds", vol. I, Butterworth Group (London, 1960), p. 326, 328.

[27] N.N. Greenwood and E.J.F. Ross, "Index of Vibrational Spectra of Inorganic and Organometallic Compounds", vol. II, Butterworth Group (London, 1963), p. 457.

[28] N.N. Greenwood and E.J.F. Ross, "Index of Vibrational Spectra of Inorganic and Organometallic Compounds", vol. III, Butterworth Group (London, 1966), p. 800, 1078.

[29] V.P. Tolstoy, I.V. Chernyshova and V.A. Skryshevsky, "Handbook of Infrared Spectroscopy of Ultrathin Films", John Wiley & Sons, Inc. (NJ, 2003), p. 435.

[30] S.-T. Xiao et al., "Rich surface hydroxyl design for nanostructured TiO_2 and its hole-trapping effect", Chem. Eng. J., 400 (2020) 125909.

[31] B. Roy and S. Aich, "Synthesis of Mixed-Phase TiO_2 Powders in Salt Matrix and Their Photocatalytic Activity", Mater. Manufact. Process., 31(12) (2016) 1628-1633.

IRAQI JOURNAL OF APPLIED PHYSICS
Vol. 18, No. 2, April-June 2022, pp. 33-36

Roban Diklar

Department of Physics,
Faculty of Science,
University of Kerala,
Kariavattom Campus,
Kerala, INDIA

Tapering and Metallizing Optical Fibers by Immersion in Buffered Aqueous Solution with Different Molar Ratios

In this work, three basic techniques for tapering an optical fiber were presented and discussed. These techniques are meniscus etching, selective etching and pulling. They depend on immersion of the optical fiber in a buffered HF solution (BHF) with different volume ratio of [40%-NH_4F aqueous sol.]:[50%-HF acid]:[H_2O] at 25°C. The dependencies of dissolution rates and cone angle on the ratio of [40%-NH_4F aqueous sol.] were determined. The dependency of cone angle on the difference in refractive index was determined too.

Keywords: Optical design; Optical fiber; Fiber tapering; Fiber metallization
Received: 08 April 2022; **Revised:** 29 April 2022; **Accepted:** 06 May 2022

1. Introduction

Optical design is the most fundamental and important step in optics, photonics and optoelectronics science and technology. There are many optical components to be included according to the required design [1-3]. For example, in laser design, the pumping design, resonator, front and rear mirrors, internal optics, manipulation optics, pulse forming technique and antireflection coatings are the most common components to be carefully chosen and optimized [4-6]. Each component is made from optical material with certain refractive index, homogeneity and thermal properties [7,8].

For tapering an optical fiber, three basic techniques, i.e., heating and pulling, meniscus etching, and selective etching have been used. In the heating-and-pulling technique [9,10], a silica-based optical fiber is heated and pulled by a micropipette puller combined with a CO_2-gas laser as shown in Fig. (1). One can fabricate a tapered fiber with an apex diameter of 50 nm and a cone angle of 20-40° by a commercial micropipette puller [11-13]. This tapering can be applied to any optical fiber with a diameter of more than 125 μm by adjusting the laser power, the strength of the pull, and the delay time between the end of the heating and the beginning of the pulling. However, it is difficult to control the cone angle while maintaining an apex diameter as small as 50 nm [14,15]. In the tapered portion, strong optical leaky modes are generated due to the varied core diameter [16,17].

For i-mode SNOM, the pulled fiber with an apex diameter of about 50 nm must be metallized except for its apex region [18,19]. To metallize the fiber, the pulled fiber is rotated while evaporating aluminum in vacuum as shown in Fig. (2a) so that the metallized probe has a thickness profile as shown in Fig. (2b). Here, the typical radial thickness is around 150 nm [20]. The apex region is aluminized with a thickness smaller than the half-radial thickness due to the throwing of evaporated vapor [21]. The metal thickness covering the apex region can be reduced to a quarter of the radial thickness by inclining the rotating fiber in vacuum [22].

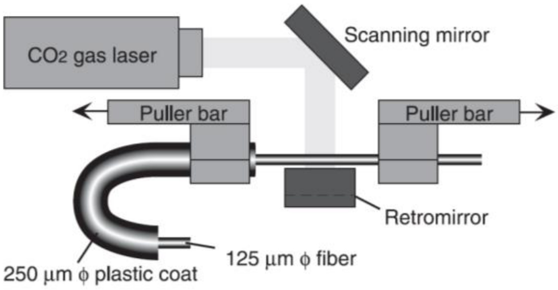

Fig. (1) Schematic illustration of the micropipette puller used for tapering an optical fiber with a diameter of 125 μm [23]

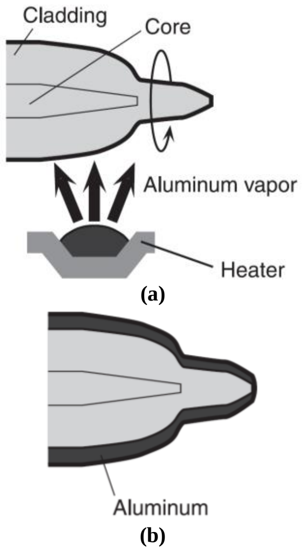

Fig. (2) Schematic illustrations of (a) the vacuum evaporation unit for metallizing the pulled optical fiber and (b) the metallized fiber [23]

Table (1) Characteristics of the three basic techniques for tapering an optical fiber [24-26]

Technique	Cone Angle (θ)	Apex Diameter (d)	Reproducibility
Meniscus etching	9-40°	≥ 60 nm	≤ 80%
Selective etching	14-180°	10 nm	≈ 100%
Pulling	20-40°	50 nm	≈ 80%

2. Experimental Work

The meniscus-etching technique was originally developed to fabricate a fiberoptic microlens. In the meniscus etching, a single-mode fiber is immersed in HF acid with a surface layer of an organic solution such as silicone oil as shown in Fig. (3a). It is tapered with a cone angle since the height of the meniscus formed around the fiber is reduced depending on the fiber diameter (Fig. 3b). When the fiber is completely tapered, the etching stops automatically (Fig. 3c). The cone angle can be increased up to 35-40°. However, the obtained tapered fiber has a geometrically eccentric apex with an elliptical cross section. The longer and shorter principal diameters of this elliptical apex take values of 200 nm and 10-20 nm, respectively.

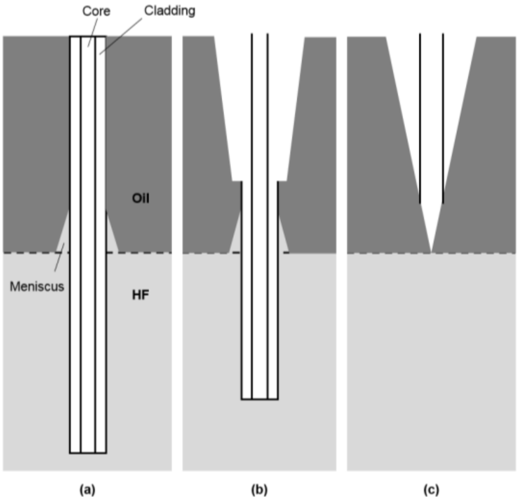

Fig. (3) Schematic illustrations of meniscus etching of a fiber at (a) the start, (b) tapering, and (c) stop

By applying the selective-etching method to a highly GeO_2-doped fiber, one can obtain probe tips with a small apex diameter less than 10 nm. By varying the concentration of etching solutions based on hydrogen fluoride (HF) and ammonium fluoride (NH4F), the cone angle can be controlled in a wide region from 20° to 180° for an apex diameter less than 10 nm. Furthermore, selective etching is the most highly reproducible technique among the three tapering techniques. This method can be applied to any single-mode fiber produced by vapor-phase axial deposition (VAD) [27].

3. Results and Discussion

Figure (4a) shows a cross-sectional profile of the refractive index of a silica fiber with a GeO_2-doped core and a pure silica clad. Here, n_1 and n_2 are the refractive indexes of the core and clad, respectively. r_1 and r_2 are the radii of the core and clad, respectively. On immersing the fiber in a buffered HF solution (BHF) with a volume ratio of [40%-NH_4F aqueous sol.]:[50%-HF acid]:[H_2O]= X:1:1 at 25°C, the core is hollowed at X = 0 and is tapered at X = 10. Figure (4b) shows a schematic explanation of the geometrical model for the tapering process based on selective etching. Bright shading and dark shading in the upper part represent the cross-sectional profiles of the fiber before and after the etching with an etching time τ, respectively. Etching time is required for making the apex diameter zero, θ and d are the cone angle and apex diameter of the probe, respectively. The lower part shows the dissolution rates R_1 and R_2 of the core and clad, respectively. Here, $R_1 < R_2$. Assuming that the dissolution rates R_1 and R_2 are constant within the core and clad regions, respectively, relations between the cone angle θ, the length L of the tapered core, and the apex diameter d are represented by [23]

$$sin\frac{\theta}{2} = \frac{R_1}{R_2} \qquad (1)$$

$$L = \frac{r_1 - \frac{d}{2}}{tan\left(\frac{\theta}{2}\right)} \qquad (2)$$

and

$$d(T) = \begin{cases} 2r_1\left(1 - \frac{T}{\tau}\right) & T < \tau \\ 0 & T \geq \tau \end{cases} \qquad (3)$$

Here, the etching time τ that is required for making the apex diameter zero is expressed as

$$\tau = \frac{r_1}{R_1}\sqrt{\frac{R_1 + R_2}{R_2 - R_1}} \qquad (4)$$

When a fiber with a GeO_2-doped core and a pure silica clad is immersed in BHFs with volume ratios of X:1:1, the core region is hollowed in $X < 1.7$, and is tapered in $X > 1.7$ as shown in Fig. (4). Based on (1), the cone angle is determined by the dissolution rate ratio of the core and clad. Figures (5) and (6) show variations of the dissolution rates R_1 and R_2 and the cone angle θ, respectively, as a function of X. Here, the fiber used was produced by vapor-phase axial deposition (VAD) so as to have an index difference of 2.5%. The dissolution rate ratio R_1/R_2 decreases with increasing NH4F volume ratio of X, and approaches a constant value at $X = 10\text{-}30$. The cone angle that is determined by the ratio R_1/R_2 takes a minimum value of 20° at $X = 10$. When X is fixed, the cone angle is determined by the index difference. Figure (7) shows the dependence of the cone angle on the index difference at $X = 10$. The index difference is increased by increasing the GeO_2 doping ratio.

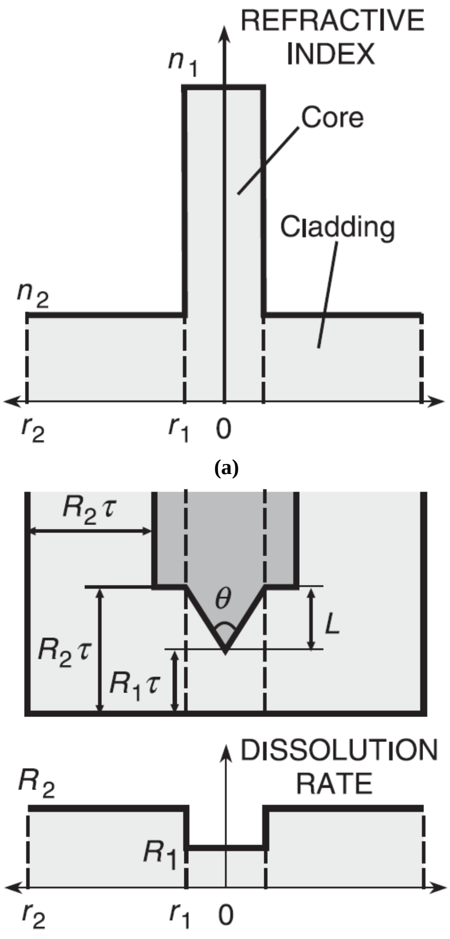

(a)

(b)

Fig. (4) (a) Cross-sectional profile of a refractive index of a silica fiber. Here, n_1 and n_2 are the refractive indices of the core and clad, respectively; r_1 and r_2 are the radii of the core and clad, respectively. (b) *Top*, a geometrical model for the tapering process; Here, τ is the etching time required for making the apex diameter zero. θ is the cone angle of the tapered core. L is the length of the tapered core. *Bottom*, cross-sectional profiles of the dissolution rates R_1 and R_2 of the core and clad

The VAD is an effective method to produce a GeO_2-doped fiber with an index difference as large as 2.5-3.0%. A dispersion-compensating fiber (DCF) with an index difference of Δn = 2.5% and core diameter of 2 µm can be applied to various selective etching methods of fabricating a protrusion-type probe, a double-tapered probe, etc. This DCF was originally produced as a device for controlling the optical dispersion of a 1500-nm optical transmission system by VAD, and has a cutoff wavelength of around 0.8 µm.

By immersing the DCF in BHF with a volume ratio of 10:1:1 at 25°C, a tapered fiber probe with a small cone angle of 20° and an apex diameter less than 10 nm is fabricated with almost 100% reproducibility. Furthermore, the cone angle can be controlled as $20° \leq \theta < 180°$ by varying the volume ratio X of BHF, as shown in Fig. (6). Such high controllability of the cone angle is indispensable for tailoring a high-throughput probe and a high-resolution probe [28].

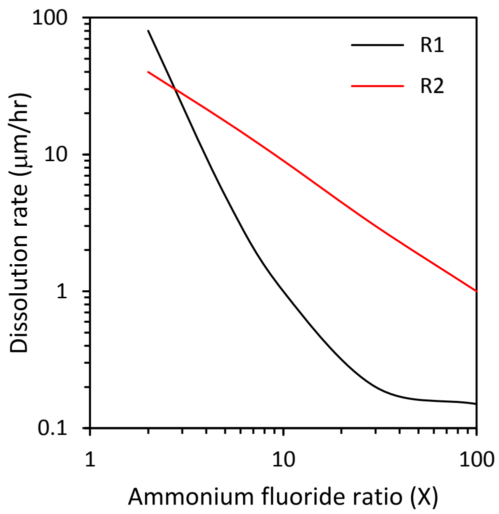

Fig. (5) Dependencies of the dissolution rate R_1 (*black line*) of the GeO_2-doped core, R_2 (*red line*) of the pure silica clad on the ratio of 40%-NH_4F aqueous solution (X)

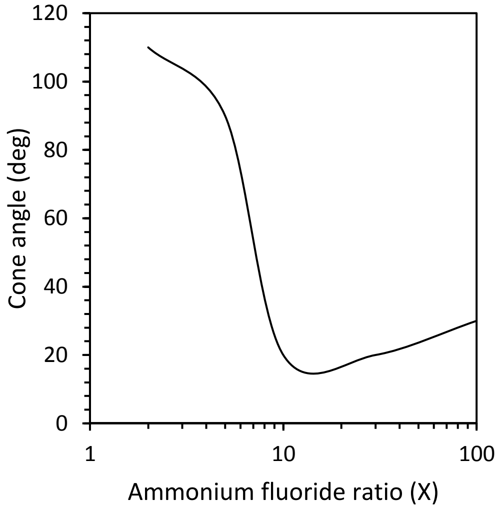

Fig. (6) Dependency of the cone angle θ on ratio of 40%-NH_4F aqueous solution (X). Here, the value of Δn defined as $(n_{21}-n_{22})/2n_{21}$ is 2.5%

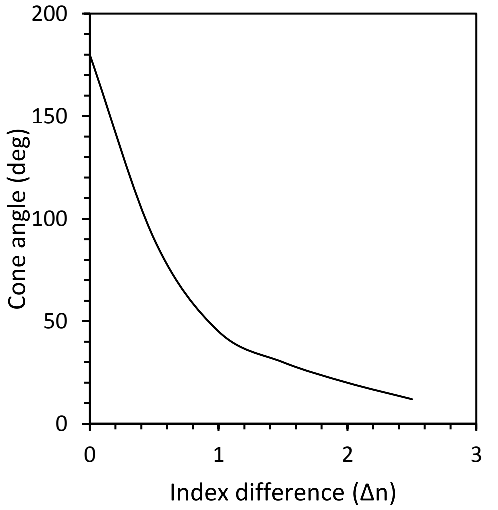

Fig. (7) Dependency of the cone angle θ on the index difference (Δn) at X = 10

4. Conclusions

In this work, three basic techniques for tapering an optical fiber were presented and discussed. These techniques are meniscus etching, selective etching and pulling. They depend on immersion of the optical fiber in a buffered HF solution (BHF) with different volume ratio of [40%-NH_4F aqueous sol.]:[50%-HF acid]:[H_2O] at 25°C. The dependencies of dissolution rates and cone angle on the ratio of [40%-NH_4F aqueous sol.] were determined. The dependency of cone angle on the difference in refractive index was determined too.

References

[1] A. Balmer et al. “Oxide-defined GaSb VCSELs on ITO substrates”, *J. Photon. Technol.*, 11 (1999) 33-36.
[2] C. Dwight et al. “Integration of III-V optoelectronic devices with Si-based circuitry”, *Opt. Res. Lett.*, 13 (2001) 55-56.
[3] E. Fowler et al. “Bubble-Free Germanium Wafer Bonding in a Non-Cleanroom Ambient”, *Czech J. Phys.*, 15 (2003) 67-70.
[4] G. Heinrisch et al. “Nickel contamination and indium segregation in directly bonded silicon wafers”, *J. Solid Stat. Opt.*, 17 (2005) 81-84.
[5] I. Jafaar et al. “Bonding of silicon wafer by novel design of monolayers”, *Acta Mater.*, 10 (2007) 103-106.
[6] K. Lancer et al. “Surface activation of silicon wafer bonding at low temperatures”, *Mater. Commun.*, 12 (2009) 21-24.
[7] M. Neumann et al. “Room-temperature semiconducting wafer bonding in high vacuum environment”, *J. Solid Stat. Technol.*, 8 (2012) 39-42.
[8] O. Parker et al. “Fusion bonding of oxidized silicon wafers at low temperatures”, *Solid Stat. Lett.*, 14 (2015) 57-60.
[9] Q. Ronahi et al. “Fusion bonding of silicon wafers in low vacuum”, *Solid Stat. Lett.*, 15 (2016) 113-116.
[10] M. Ohtsu, **“Progress in Nano-Electro-Optics III”**, Springer (Berlin, 2005), p. 8.
[11] S. Tucker et al. “Fusion bonding of silicon wafers with polymer thin films at room temperature”, *Acta Mater.*, 13 (2010) 207-210.
[12] U. Vlahovich et al. “Low-dark-current wafer-bonded Si/InSb photodiodes”, *J. Photon. Technol.*, 17 (2005) 311-314.
[13] W. Xu et al. “Fusion-bonded InSb wafers for photonics networks”, *Opt. Res. Lett.*, 22 (2010) 125-128.
[14] Y. Zhang et al. “Room-temperature fusion bonding technology for photonics networks”, *Opt. Res. Lett.*, 23 (2011) 103-106.
[15] A. Zahidi et al. “Chemical cleaning of InSb(100) surfaces in HF solutions”, *Opt. Mater. Lett.*, 26 (2004) 13-16.
[16] Y. Bond et al. “Chemical cleaning of GaSb(100) surfaces in aqueous solutions”, *Opt. Mater. Lett.*, 27 (2005) 215-218.
[17] C. Xiao et al. “SIMS analysis of HF/UV treated silicon (100) surfaces”, *Solid Stat. Lett.*, 18 (2019) 69-72.
[18] W. Dillan et al. “Ohmic conduction across wafer-bonded compound semiconducting interfaces”, *Acta Mater.*, 22 (2019) 441-444.
[19] E. Varner et al. “Self-propagating low-temperature germanium wafer bonding”, *Solid Stat. Lett.*, 21 (2021) 355-358.
[20] U. Fitzgerald et al. “High bonding energy and thermal stress in silicon on ITO wafer bonding”, *Solid Stat. Lett.*, 21 (2021) 467-470.
[21] G. Tayeb et al. “Hetero-interface silicon photodetector with high gain-bandwidth-product”, *Opt. Res. Lett.*, 32 (2021) 327-330.
[22] S. Hömels et al. “Direct wafer bonding for super-junction fabrication”, *Photon. Opto. Lett.*, 19 (2020) 143-146.
[23] I. Reynolds et al. “Non-destructive measurements of wafer-bonded surface energy”, *Photon. J. Photon. Technol.*, 31 (2019) 1219-1222.
[24] Q. Jong et al. “Electrical characteristics of CdS/Si heterojunction solar cells under radiation effect”, *J. Photon. Technol.*, 25 (2020) 129-132.
[25] K. Poles et al. “Fabrication of CdS/Si heterojunction solar cells by chemical bath method”, *Solid Stat. Lett.*, 20 (2020) 277-280.
[26] O. Leon et al. “Deposition of CdSe thin films on ITO substrates by PLD method”, *Prog. Mater. Phys.*, 12 (2018) 45-48.
[27] M. Nabawi et al. “Wafer-bonding fabrication of InSb/InP heterostructures on silicon substrates”, *Prog. Mater. Phys.*, 13 (2019) 123-126.
[28] N. Müller et al. “Wafer-bonding of InGaP thin films on (100) silicon substrates”, *Prog. Mater. Phys.*, 14 (2020) 257-260.

THE IRAQI JOURNAL OF APPLIED PHYSICS
EDITORIAL BOARD

COPYRIGHT RELEASE FORM
IRAQI JOURNAL OF APPLIED PHYSICS (IJAP)

We, the undersigned, the author/authors of the article titled
………
………
………
………
………
………
………

that is submitted to the Iraqi Journal of Applied Physics (IJAP) for publication, declare that we have neither taken part or full text from any published work by others, nor presented or published it elsewhere in any other journal. We also declare transferring copyrights and conduct of this article to the Iraqi Journal of Applied Physics (IJAP) after accepting it for publication.

The authors will keep the following rights:
1. Possession of the article such as patent rights.
2. Free of charge use of the article or part of it in any future work by the authors such as books and lecture notes after informing IJAP editorial board.
3. Republishing the article for any personal purposes of the authors after taking journal permission.

To be signed by all authors:

Signature:…………………………………………………………..date: …………………………………………
Printed name: ………………………………………………………………………………………………………

Signature:…………………………………………………………..date: …………………………………………
Printed name: ………………………………………………………………………………………………………

Signature:…………………………………………………………..date: …………………………………………
Printed name: ………………………………………………………………………………………………………

Correspondence
address:……………………………………………………………………………………………………..
………
Address:………
………
Telephone:…………………………………………….email: ……………………………………………………

Note: Complete and sign this form and mail it to the below address with your finally revised manuscript

The Iraqi Journal of Applied Physics
www.iraqiphysicsjournal.com
Email: info@iraqiphysicsjournal.com
Email: editor_ijap@yahoo.co.uk
Email: ijap.editor@gmail.com

IRAQI JOURNAL OF APPLIED PHYSICS

Volume (18) Issue (2) April-June 2022

CONTENTS